https://doi.org/10.5194/egusphere-2025-2197
Preprint. Discussion started: 14 July 2025

MONKI: a three-dimensional Monte Carlo simulator of total and polarised radiation reflected by planetary atmospheres

Victor J. H. Trees [1,2], Ping Wang [2], Job I. Wiltink [2,3], Piet Stammes [2], Daphne M. Stam [4], David P. Donovan [2], and A. Pier Siebesma [1]

[1]Geoscience and Remote Sensing Department, Delft University of Technology, Delft, the Netherlands
[2]R&D Satellite Observations, Royal Netherlands Meteorological Institute (KNMI), De Bilt, the Netherlands
[3]Meteorology and Air Quality Group, Wageningen University & Research, Wageningen, the Netherlands
[4]Leiden Observatory, Leiden University, Leiden, the Netherlands

Correspondence: Victor Trees (v.j.h.trees@tudelft.nl)

Abstract.

Spectropolarimetry is a powerful tool for characterising planetary atmospheres and surfaces. For the design and operation of spectro(polari)metric instrumentation, numerically simulated signals of the measured radiation are essential. Here we present MONKI (Monte Carlo KNMI), an efficient and accurate radiative transfer code written in Fortran, based on the Monte Carlo method. MONKI computes both total and polarised radiances reflected and transmitted by a planetary atmosphere, fully accounting for the polarisation of light in all orders of scattering. MONKI can handle atmospheres that are horizontally homogeneous, as well as those with horizontal inhomogeneities, such as three-dimensional (3D) patchy clouds. We validate MONKI through comparisons with various other radiative transfer codes and demonstrate that it converges reliably even for optically thick and strongly polarising atmospheres. Finally, we present sample simulations of sunlight reflected by the Earth and Venus, and explain the total and polarised radiance features by analysing the altitudes at which the photons are scattered. We conclude that MONKI is a versatile and accurate tool, suitable for simulations and detailed analyses of locally reflected light by the Earth, Venus, and, in principle, any other planet.

1 Introduction

Sunlight and, more generally, starlight of solar-type stars, can be considered to be unpolarised when integrated over the disk (Kemp et al., 1987). This light becomes (partially) polarised when it is scattered by the particles constituting a planetary atmosphere. Measuring the degree of polarisation, P, of the scattered light, i.e., the amount of polarised radiance w.r.t. the total radiance, is a powerful tool to characterise planetary atmospheres because P is very sensitive to the scattering angles, the wavelength of the light, and the composition, size, and shape of the scattering particles (Hansen and Travis, 1974). If a planetary atmosphere is bounded below by a surface, light that has been reflected by the surface can also influence the polarisation of the light that is reflected by the planet at the top of at the atmosphere (TOA), depending on optical properties of the surface. In particular, Fresnel reflection by liquid surfaces (water on Earth, but methane on Titan) or leaves of vegetation can strongly

https://doi.org/10.5194/egusphere-2025-2197
Preprint. Discussion started: 14 July 2025

polarise the light (see e.g. Mishchenko and Travis, 1997; Vanderbilt et al., 1985). Additionally, since P is a relative measure, it is insensitive to various instrumental errors and to uncertainties in the total flux of the light that is incident at TOA.

An example of an Earth-observation satellite instrument dedicated to measuring the degree of polarisation was the POLarisation and Directionality of the Earth's Reflectances (POLDER) imager (Deschamps et al., 1994). With multi-angular polarisation observations across three spectral bands, it provided an alternative for cloud droplet size retrieval compared to traditional methods relying solely on total radiances (Breon and Doutriaux-Boucher, 2005), and improved the capability to characterise aerosols above liquid water clouds (Waquet et al., 2013). In February 2024, NASA launched the Plankton, Aerosol, Cloud, Ocean Ecosystem (PACE) satellite (Werdell et al., 2019), carrying the Hyper-Angular Rainbow Polarimeter-2 (HARP-2) (McBride et al., 2024) and the SPEXone spectropolarimeter (van Amerongen et al., 2019), enabling accurate global polarisation measurements of aerosols and clouds to better quantify their impact on radiative forcing. Upcoming spaceborne Earth observation polarimeters are the Multi-Viewing Multi-Channel Multi-polarisation Imaging mission (3MI) on METOP-SG (Meteorological Operational Satellite - Second Generation) planned for 2025 (Marbach et al., 2015), and the Multi-Angle Polarimeter (MAP) on the Copernicus Anthropogenic Carbon Dioxide Monitoring (CO2M) mission that is scheduled for launch in 2026 (Spilling and Thales, 2021).

Polarimetry has also proven its strength in characterising other solar system bodies than the Earth (see Bagnulo et al., 2024, and references therein). A famous example is the characterisation of Venus's main cloud deck by Hansen and Hovenier (1974), who found that the droplets consist of a $\sim$75% H_2SO_4 mixture with water, and that their sizes are described by a narrow distribution and effective radii of $\sim$1 μm radius. They achieved this characterisation using ground-based polarisation measurements of Venus (spatially unresolved, thus integrated across the planet's disk) at a number of wavelengths and a range of planetary phase angles (that is, the angles between Earth, Venus and the Sun) collected over decades by several different observers. ESA's upcoming Venus orbiter EnVision (Ghail et al., 2021), planned for launch in 2032, will carry VenSpec-H (Neefs et al., 2025), a near-infrared spectrometer that will include polarisation filters. These filters will be used to correct for VenSpec-H's polarisation sensitivity (i.e. the instrument response depends on the polarisation of the observed light) and can also be used to characterise Venus's clouds and hazes in unprecedented detail. Beyond our solar system, polarimetry has been proposed to detect liquid water clouds (Stam, 2008; Karalidi et al., 2011; Rossi et al., 2022) and liquid water oceans (Trees and Stam, 2019, 2022) on exoplanets, for example with NASA's upcoming space-borne Habitable Worlds Observatory (HWO) (Vaughan et al., 2023).

Radiative transfer simulations of reflected (polarised) light are essential for spectro(polari)meters on space missions. Simulations (1) help explore the observational parameter space during the design phase, (2) serve as sample signals for the development of end-to-end data simulations, and (3) form the core of atmospheric retrieval algorithms during space mission operations. For instruments that are polarisation sensitive, simulations are used to estimate the impact of the sensitivity on the total radiance measurements. Even for instruments with a polarisation scrambler, such as TROPOMI (Veefkind et al., 2012), accounting for polarisation in radiative transfer simulations remains important for accurate total radiance estimations. This is because atmospheric scattering is only properly described by a (phase) matrix multiplication of the Stokes vector, not by a scalar (phase function) multiplication of the radiance (see Chandrasekhar, 1960; van de Hulst, 1981; Hovenier et al., 2004). Neglecting

https://doi.org/10.5194/egusphere-2025-2197
Preprint. Discussion started: 14 July 2025

(linear) polarisation can cause errors of more than 9% in the computed geometric albedo of planets with Rayleigh scattering atmospheres (Stam and Hovenier, 2005), and up to 10% in the computed locally reflected radiance for cloud-free atmospheres (Mishchenko et al., 1994) and 8% in patchy cloudy conditions (Emde and Mayer, 2018), depending on the wavelength and scattering geometry.

Several types of radiative transfer algorithms can simulate both the total and polarised radiances reflected by scattering planetary atmospheres. Classical radiative transfer codes divide the atmosphere into horizontally homogeneous, plane-parallel layers, computing the signal at the top of the atmosphere (TOA) using e.g. the doubling-adding method (de Haan et al., 1987) or the discrete-ordinates method (Chandrasekhar, 1960). Despite advances in radiative transfer simulations and computing power, most satellite retrieval algorithms for aerosols, clouds and trace gases still rely on this horizontally homogeneous approach, due to its simplicity, efficiency, and the limited availability of knowledge about the scene's inhomogeneity. For instance, the aerosol retrieval algorithm of SPEXone applies an independent pixel approximation (IPA), modelling the signal of a partly cloudy pixel as a weighted sum of horizontally homogeneous cloud-free and fully cloudy scenes (see Hasekamp, 2010; Hasekamp et al., 2019).

In reality, planetary atmospheres are usually horizontally inhomogeneous. In particular, 3D cloud structures can cast shadows onto the surface or lower atmospheric layers, and/or scatter light towards cloud-free regions (see, e.g. Marchand and Ackerman, 2004; Marshak and Davis, 2005; Marshak et al., 2006), thus affecting observations from imagers such as MODIS (Wen et al., 2013; Várnai et al., 2013). Furthermore, 3D cloud effects can introduce significant errors in aerosol retrievals, as shown by Stap et al. (2016a, b) and Cornet et al. (2018) for POLDER observations over broken cloud decks. Although spectro(polari)meters typically have larger pixels than imagers, Trees et al. (2022) detected cloud shadows in radiance measurements by the TROPOMI spectrometer which has a pixel size of 5.5×3.5 km^2 in the nadir viewing direction. As the spatial resolution of spectro(polari)metric instruments continues to increase, understanding and correcting for these 3D effects becomes increasingly important.

Examples of radiative transfer codes capable of simulating both total and polarised radiances while accounting for the 3D structure of the atmosphere are 3DMCPOL (Cornet et al., 2010; Fauchez et al., 2014), MSCART (Wang et al., 2017), MYSTIC (Mayer, 2009; Emde et al., 2010), SHDOM (Evans, 1998), and SPARTA (Barlakas et al., 2016). Most of these codes (except SHDOM) use the Monte Carlo method, simulating light as the statistical propagation of photon packets through a model atmosphere. Their simulated total and polarised radiances have been compared (Emde et al., 2018). We note that these codes have primarily been applied to model scenarios on Earth. An example of a polarised 3D radiative transfer code for simulating sunlight reflected by other planets than the Earth is the Preconditioned Backward Monte Carlo (PBMC) algorithm of García Muñoz and Mills (2015). Unlike classical Monte Carlo codes, PBMC converges even in optically thick and strongly polarising atmospheres, such as that of Venus, by fully accounting for the photon's polarisation state history along its path.

In this paper, we present MONKI (Monte Carlo KNMI), a 3D Monte Carlo code for simulating total and polarised radiances that are locally reflected or transmitted by planetary atmospheres. MONKI can perform simulations in both forward and backward modes (with reversed photon directions) for horizontally homogeneous and inhomogeneous (3D cloudy) scenes. MONKI is designed for versatility, accepting input model atmospheres and surfaces for any planet. For Earth-based applica-

https://doi.org/10.5194/egusphere-2025-2197
Preprint. Discussion started: 14 July 2025

tions, MONKI computes atmospheric optical properties identically to DAK (Doubling Adding KNMI) (de Haan et al., 1987; Stammes, 2001) and has already been used to simulate cloud shadow effects in TROPOMI's Absorbing Aerosol Index product (Trees et al., 2025). By fully tracking the polarisation state history of photons along their paths, MONKI also converges in optically thick and strongly polarising planetary atmospheres. The code has been written in Fortran-90.

This paper is organised as follows. In Sect. 2, we describe the MONKI algorithm. In Sect. 3, we validate MONKI through comparisons with results of other radiative transfer codes. In Sect. 4, we show sample simulations of total radiances and the degree of polarisation for locally reflected light from Earth and Venus. In Sect. 5, finally, we provide a summary, discussion, and outlook. The appendices contain derivations and detailed explanations of the formulae implemented in MONKI.

2 Method

2.1 Definitions of TOA reflectance and polarisation

The radiance and polarisation state of a light beam can be described by a Stokes vector (see, e.g., Hansen and Travis, 1974; Hovenier et al., 2004)

$$\boldsymbol{I} = [I, Q, U, V]^T, \tag{1}$$

where I is the total radiance (or intensity), Q and U are the linearly polarised radiances, and V is the circularly polarised radiance. All radiances are expressed in units of W m^{-2} nm^{-1} sr^{-1}, where nm^{-1} indicates the dependence on the wavelength of light, λ, and sr^{-1} indicates the dependence on the solid angle, Ω. The linearly polarised radiances, Q and U, are defined relative to a reference plane. For example, for light that is reflected locally by the planet, the local meridian plane can be used, which contains the local zenith direction and the direction of light propagation towards the observer (see de Haan et al., 1987).

The sunlight incident at the top of the atmosphere of a planet is assumed to be unpolarised (Kemp et al., 1987), and is represented by the following Stokes vector

$$\boldsymbol{E_0}(\lambda) = [E_0(\lambda), 0, 0, 0]^T, \tag{2}$$

expressed in W m^{-2} nm^{-1}. In Earth observation studies, the wavelength-dependent total solar flux, $E_0(\lambda)$, is commonly known as the 'irradiance spectrum'. The incident sunlight is also assumed to be unidirectional, leading to the following expression for the Stokes vector of the light that is locally reflected by the planetary atmosphere-surface system (thus at TOA) (see Hansen and Travis, 1974)[1]

$$\boldsymbol{I}(\mu, \mu_0, \varphi, \varphi_0, \lambda) = \frac{\mu_0}{\pi} \boldsymbol{R}(\mu, \mu_0, \varphi, \varphi_0, \lambda) \boldsymbol{E}_0(\lambda), \tag{3}$$

where $\boldsymbol{R}$ denotes the 4 $\times$ 4 reflectance matrix of the local atmosphere-surface system. We use the quantities $\mu = |\cos\theta|$ and $\mu_0 = |\cos\theta_0|$, where θ ($0 \leq \theta \leq \pi$) and θ_0 ($0 \leq \theta_0 \leq \pi$) represent the local viewing and solar zenith angles, respectively,

[1] Hansen and Travis (1974) used the notation $\pi \boldsymbol{F}_0$ instead of $\boldsymbol{E}_0$ for the solar flux vector.

https://doi.org/10.5194/egusphere-2025-2197
Preprint. Discussion started: 14 July 2025

measured positively from the local zenith (i.e., the z-axis). Angles φ ($0 \leq \varphi \leq 2\pi$) and φ_0 ($0 \leq \varphi_0 \leq 2\pi$) are the local viewing and solar azimuth angles, respectively. They are defined relative to the x-axis of the local Cartesian coordinate system, and are measured in the clockwise sense when looking in the local zenith direction, as illustrated in Fig. 1.

Light in the local atmosphere-surface system usually becomes polarised upon scattering, leading to non-zero values of Q, U and/or V. From Eq. 3 it follows that the assumption of the unpolarised incident sunlight implies that only the first column of $\boldsymbol{R}$, thus $[R_{11}, R_{21}, R_{31}, R_{41}]^T$, contributes to $\boldsymbol{I}$. Combining Eqs. 2 and 3, and omitting the explicit dependencies on angles and wavelengths, we arrive at

$$\begin{bmatrix} R_{11} \\ R_{21} \\ R_{31} \\ R_{41} \end{bmatrix} = \frac{\pi}{\mu_0 E_0} \begin{bmatrix} I \\ Q \\ U \\ V \end{bmatrix}, \tag{4}$$

where the element R_{11} is referred to as the total TOA reflectance, R_{21} and R_{31} as the linearly polarised TOA reflectances, and R_{41} as the circularly polarised TOA reflectance. Those TOA reflectances are independent of E_0, and their (angular and wavelength dependent) values are determined by the composition of the local atmosphere and surface. Similar definitions can

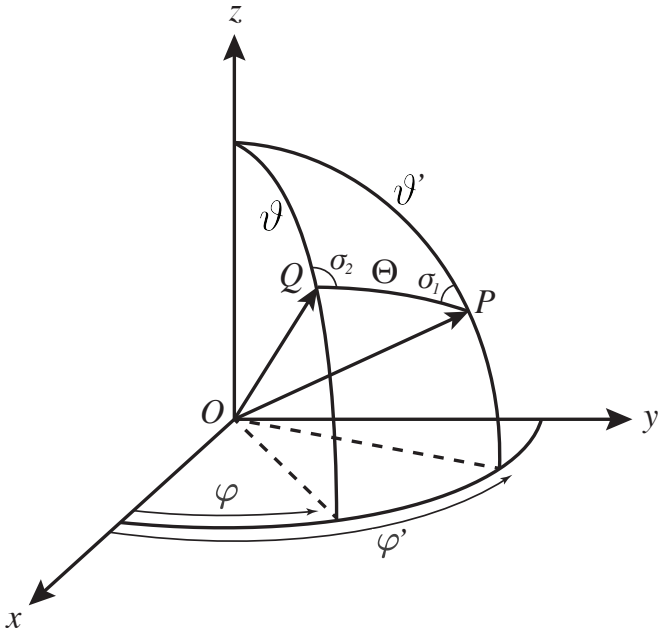

Figure 1. The reference system used in MONKI. The incident light with propagation direction OP is scattered at O into direction OQ over scattering angle Θ. The azimuthal angles for the incident and scattered light are denoted by φ' and φ, respectively. The zenith angles of the incident and scattered light are ϑ' and ϑ, respectively. In the case of incident and reflected (or transmitted) light at TOA (or BOA), the solar and viewing azimuth and zenith angles are defined as $\varphi_0 = \varphi'$, $\theta_0 = 180° - \vartheta'$, $\varphi = \varphi$, and $\theta = \vartheta$. Angles σ_1 and σ_2 are the angles between the meridian planes of the incident and scattered light, respectively, with OPQ the scattering plane.

https://doi.org/10.5194/egusphere-2025-2197
Preprint. Discussion started: 14 July 2025

be derived for the transmittance at the bottom of the atmosphere (BOA), by replacing $\boldsymbol{R}$ in Eq. 3 with $\boldsymbol{T}$, the 4×4 transmission matrix of the local atmosphere.

The polarisation of the reflected or transmitted light beam can be quantified by its degree of polarisation P:

$$P = \frac{\sqrt{Q^2 + U^2 + V^2}}{I}. \tag{5}$$

The degree of polarisation is independent of the choice of reference plane. When $U = 0$, we can use an alternative definition that includes the direction of polarisation:

$$P_\mathrm{s} = -Q/I. \tag{6}$$

When P_s is positive (negative), the light is polarised perpendicularly (parallel) to the reference plane. Because P and P_s are relative measures, they are both independent of the incoming solar flux E_0.

2.2 Model grid and coordinate system

The local atmosphere-surface coordinate system is Cartesian, with the z-axis pointing towards the local zenith and the x- and y-axes oriented horizontally, as shown in Fig. 1. The model atmosphere-surface system is a 3D domain composed of N_x and N_y columns in the x and y directions, and N_z layers in the z direction. The domain is cyclic in the horizontal directions: light emerging from one horizontal boundary re-enters the domain through the opposite boundary. The observer and light source are considered infinitely far from the domain, resulting in identical values of θ, θ_0, φ, and φ_0 for all grid cells.

2.3 Calculating the reflected and transmitted sunlight

MONKI computes the total and polarised TOA reflectances and BOA transmittances of an atmosphere-surface system, using the Monte Carlo method (see, e.g., Marshak and Davis, 2005): "photons" are traced through the system.[2] Since MONKI fully accounts for the polarisation of light, a photon is represented by a normalised Stokes vector, $\overline{\boldsymbol{I}} = [1, \overline{Q}, \overline{U}, \overline{V}]^T$, carrying a weight, w, representing the probability of 'survival' of the photon (i.e., w will become zero upon absorption). The trajectory of a photon is summarised in the flow diagram in Fig. 2, which is explained below.

The photons begin their trajectory as solar irradiance photons (with $\overline{Q} = \overline{U} = \overline{V} = 0$ and $w = 1$) at TOA where they are injected into the direction of propagation of the sunlight at random x, y-locations into the grid cells. Before a photon moves through the domain, the free photon path d, that is, the straight photon path length through the grid cell until an atmospheric event (i.e., a scattering or absorption) is sampled as follows (see App. B):

$$d = \frac{-\ln(\xi_1)}{\beta}, \tag{7}$$

where ξ_1 is a random number in the open interval $(0, 1)$, drawn from a uniform distribution. Quantity β is the atmospheric extinction coefficient in m^{-1} which depends on the vertical optical thickness b and the vertical extent Δz of the grid cell

[2]Note that photons in a Monte Carlo radiative transfer simulation do not represent actual quanta of the electromagnetic field, but rather are numerical entities used to simulate the light path in a statistical manner.

https://doi.org/10.5194/egusphere-2025-2197
Preprint. Discussion started: 14 July 2025

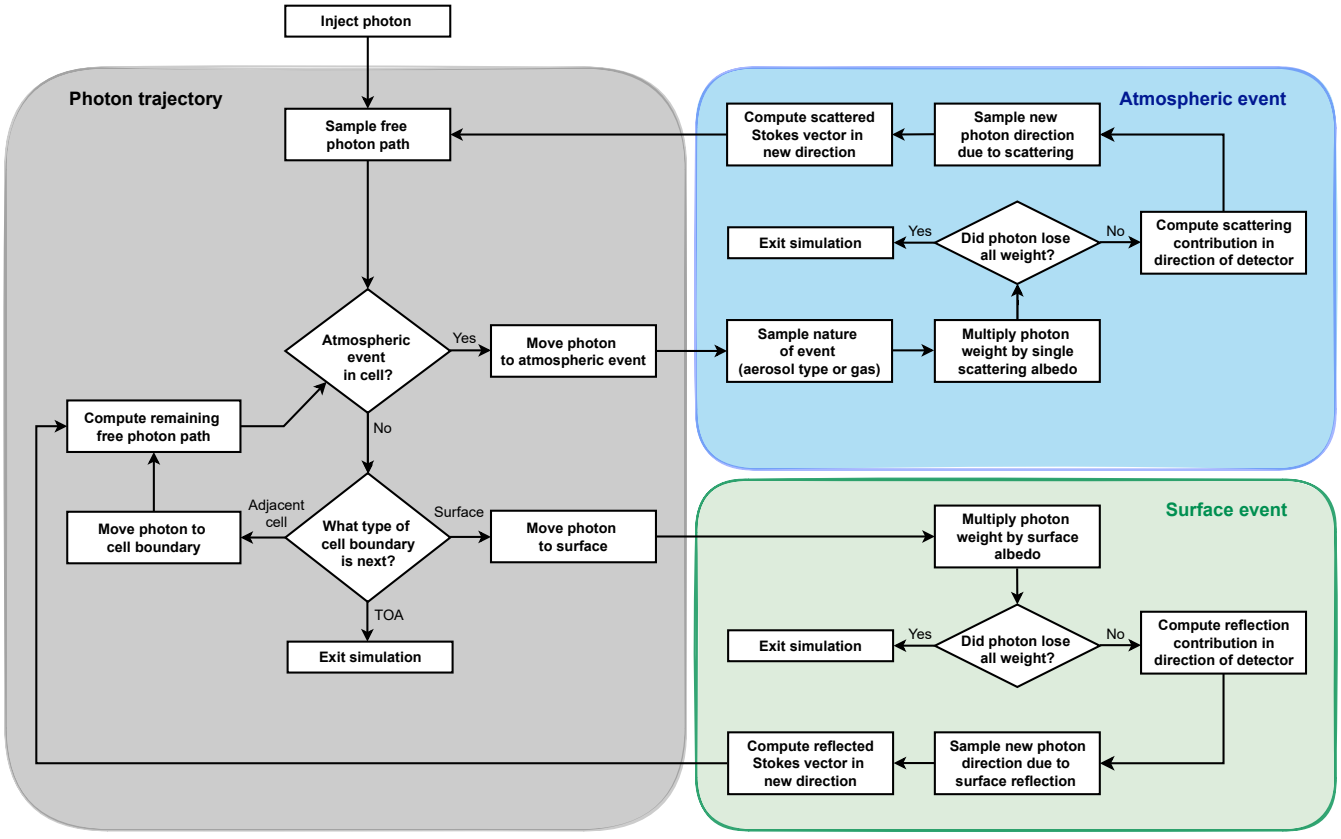

Figure 2. Flow diagram of a photon trajectory in MONKI. The boxes in the grey area pertain to the path of the photon through the atmosphere-surface domain, while the boxes in the blue and green areas represent interactions with the atmosphere and surface, respectively.

via $\beta = b/\Delta z$. The wavelength dependence and spatial distribution of b throughout the 3D grid depend on the scattering and absorption optical thicknesses of the gases and aerosol particles (see Appendix A for a description of the model atmosphere).

Next, d is compared with the distance along the straight photon path to the boundary of the grid cell, to check whether the atmospheric event occurs in the current cell. If so, the photon is moved to the atmospheric event location. If not, the photon is moved along its straight path to the grid cell boundary. The grid cell boundary may be (1) the surface, (2) TOA where the photon leaves the simulation, or (3) the boundary of an adjacent grid cell. In the latter case, the free photon path distance that remains after reaching the boundary is rescaled using the β value of the adjacent grid cell.

If an atmospheric event occurs, the photon interacts with an atmospheric particle, which can be either a gas molecule or an aerosol particle of one of the n_c types found in the grid cell. To determine which particle type is encountered, we draw a uniformly distributed random number ξ_2 between 0 and 1 and solve the following equation for j (see, e.g., Eq. 18 of Barker

https://doi.org/10.5194/egusphere-2025-2197
Preprint. Discussion started: 14 July 2025

et al., 2003):

$$\sum_{i=1}^{j-1}\frac{\beta_i}{\beta} \le \xi_2 < \sum_{i=1}^{j}\frac{\beta_i}{\beta}, \tag{8}$$

where β_i is the total extinction coefficient of a certain aerosol type ($i = 1, ..., n_c$) or of the mixture of scattering gas molecules ($i = n_c + 1$) in the grid cell. Here, β is again the total extinction of all aerosols and the gas in the grid cell: $\beta = \sum_{i=1}^{n_c+1}\beta_i$.

In an atmospheric event, the photon is either absorbed or scattered. The probability of scattering is, by definition, equal to the single scattering albedo. Therefore, instead of removing the photon from the cell upon absorption, we apply a more efficient approach: multiplying the weight w by the single scattering albedo. For molecular scattering, w is multiplied by the molecular single scattering albedo a^{m} (see Appendix A). For aerosol scattering, w is multiplied by the single scattering albedo a^{c} of the type of aerosol. If the photon lost all its weight[3], the photon exits the simulation. Otherwise, its contribution to the TOA reflectance or BOA transmittance for this scattering event is computed, as explained below.

Instead of collecting photons within the narrow solid angle subtended by the detector, MONKI uses the more efficient 'local estimation method' (Marchuk et al., 1980; Marshak and Davis, 2005), a standard approach in Monte Carlo radiative transfer algorithms (see, e.g., Spada et al., 2006; Mayer, 2009; Deutschmann et al., 2011). In this method, the photon is used to simulate the signal contributions of all atmospheric scattering and surface reflection events along the photon's trajectory. The contribution of an event to the TOA reflectance or BOA transmittance is expressed by the column vector $\boldsymbol{\Phi}$:

$$\boldsymbol{\Phi} = w \cdot \boldsymbol{\chi} \cdot \overline{\boldsymbol{I}} \cdot \exp\left(-\int_0^{s_{\mathrm{det}}} \beta(s')ds'\right), \tag{9}$$

where the exponential term represents the direct transmittance along the straight path s' from the event location ($s = 0$) to the detector ($s = s_{\mathrm{det}}$), and $\boldsymbol{\chi}$ is the 4×4 normalised phase matrix, representing the probability density function of the photon scattering (or surface reflection) direction towards the detector. MONKI can, in practice, compute the result simultaneously for multiple viewing zenith angles, that is, for multiple detector locations as seen from the event location.

In the case of an atmospheric event, $\boldsymbol{\chi}$ is computed as:

$$\boldsymbol{\chi} = \frac{1}{4\pi}\boldsymbol{L}(-\sigma_2)\boldsymbol{F}(\Theta, \lambda)\boldsymbol{L}(-\sigma_1), \tag{10}$$

where $\boldsymbol{F}$ is the single scattering matrix of the gas or the aerosol type (see Appendix A), and $\boldsymbol{L}$ is the 4×4 rotation matrix that transforms the Stokes vector between different reference planes (see Hovenier and van der Mee, 1983):

$$\boldsymbol{L}(\alpha) = \begin{pmatrix} 1 & 0 & 0 & 0 \\ 0 & \cos 2\alpha & \sin 2\alpha & 0 \\ 0 & -\sin 2\alpha & \cos 2\alpha & 0 \\ 0 & 0 & 0 & 1 \end{pmatrix}. \tag{11}$$

The rotation angle α is positive in the anti-clockwise direction when viewed along the direction of light propagation. Specifically, angles $-\sigma_1$ and $-\sigma_2$ in Eq. 10 are the angles required to rotate the reference plane from the local meridian plane of

[3]We set $w = 10^{-16}$ as the minimum allowable weight.

https://doi.org/10.5194/egusphere-2025-2197
Preprint. Discussion started: 14 July 2025

the incident beam, through the scattering plane, to the local meridian plane of the scattered beam (see Fig. 1). Matrix $\boldsymbol{\chi}$ thus generally depends on the angles that describe the new direction of the photon: ϑ and φ (see Fig. 1).

If the photon reaches the surface, w is multiplied by the surface albedo, A_s, which equals the probability of reflection by the Lambertian surface. If the photon retains weight and the observer is not at BOA, the surface reflection contribution to the TOA reflectance is computed, again using Eq. 9. For reflection by a Lambertian surface, matrix $\boldsymbol{\chi}$ is given by:

$$\boldsymbol{\chi} = \begin{pmatrix} \mu/\pi & 0 & 0 & 0 \\ 0 & 0 & 0 & 0 \\ 0 & 0 & 0 & 0 \\ 0 & 0 & 0 & 0 \end{pmatrix}, \tag{12}$$

where μ/π corresponds to the probability density function of the Lambertian surface reflection direction (see Eq. C3).

After computing the event's contribution to the TOA reflectance or BOA transmittance, the new direction of the photon, (ϑ, φ), is sampled from the probability density function of the scattering (or surface reflection) direction. To sample this new direction, we apply either the inverse transform method or the acceptance-rejection method depending on the type of event, fully accounting for the photon's state of polarisation along its trajectory (see Appendices C, D, E, and F for details on those methods and the choice of method). For the continuation of the photon's trajectory in its new direction, its Stokes vector is adjusted as follows:

$$\boldsymbol{I} = \boldsymbol{\chi}(\vartheta, \varphi)\overline{\boldsymbol{I}}, \tag{13}$$

where $\overline{\boldsymbol{I}}$ is the normalised Stokes vector of the photon before the event and matrix $\boldsymbol{\chi}$ is now computed for the new direction of the photon, (ϑ, φ). Subsequently, the scattered (or reflected) vector is normalised again by its first element: $\overline{\boldsymbol{I}} = \boldsymbol{I}/I$. Indeed, the first element of $\overline{\boldsymbol{I}}$ remains equal to 1, as the directional dependence of I is already taken care of in the sampling of the new photon direction, while the probability of scattering (or surface reflection) instead of absorption at each event is captured by w. Next, a new free photon path length d is sampled using Eq. 7 in case of an atmospheric event, or the remaining free photon path is computed in case of a surface event. The photon continues its trajectory, where it again may be (partially) absorbed, scattered by an atmospheric particle, or reflected by the surface.

Finally, the TOA reflectance column vector of a given (x, y)-grid column is computed as

$$[R_{11}, R_{21}, R_{31}, R_{41}]^T = \frac{\pi}{\mu} \frac{\sum_{i=1}^{N} \sum_{j=1}^{M} \boldsymbol{\Phi}_{i,j}}{N}, \tag{14}$$

where the summation is performed over all M scattering events (including surface reflection events) of all N photons that were injected into the column at TOA. A similar equation applies for the transmittance at BOA, which is obtained by replacing R with T. The factor π arises from the definition of the TOA reflectance, while μ accounts for the angle between the direction of the reflected light and the horizontal grid at TOA. In Appendix G, we use a simple example to validate the inclusion of π and μ.

https://doi.org/10.5194/egusphere-2025-2197
Preprint. Discussion started: 14 July 2025

2.4 Precomputation of optical paths to the detector

The extinction coefficient β in Eq. 9 depends on the position s' along the path of the photon between the event and the detector. Coefficient β may vary across grid cells within the 3D domain. Moreover, the lengths of the different path segments within each grid cell depend on both the location of the event and the viewing geometry. The integral in Eq. 9 can be numerically evaluated by propagating the photon from the event's location to the detector, obtaining β and the path segment length for each grid cell.

This evaluation is computationally expensive, as it must be performed for all events of each photon and every viewing zenith angle of the detector. However, if the path to the detector passes through atmospheric grid cells that have the same optical properties in the horizontal directions, the horizontal cell boundaries can be neglected, as only the extinction coefficient β and the path segment length per layer are relevant. If the event occurs at the surface or exactly at the bottom boundary of a layer, while the detector is above TOA, then Eq. 9 simplifies to:

$$\mathbf{\Phi} = w \cdot \boldsymbol{\chi} \cdot \overline{\boldsymbol{I}} \cdot \exp\left(-\frac{1}{\mu}\sum_{k=k^*}^{N_z} \beta_k \Delta z_k\right), \tag{15}$$

where k^* denotes the index of the layer where the event happens and $\Delta z_k/\mu$ is the path segment length through layer k in the direction from the event to the detector. Note that $\frac{1}{\mu}\sum_{k=k^*}^{N_z} \beta_k \Delta z_k$ can be computed for each k^* prior to simulating the photon trajectories. If the event occurs within the atmosphere and not exactly at a layer boundary (as is most often the case), the photon is first propagated by a distance Δs toward the detector until it reaches the nearest layer boundary. The term $\beta_{k^*}\Delta s$ is then added to $\frac{1}{\mu}\sum_{k=k^*+1}^{N_z} \beta_k \Delta z_k$. A similar approach applies for a detector below BOA.

In 3D cloudy scenes, there are still many cloud-free paths between atmospheric or surface events and the detector, for example, when events occur in atmospheric layers above the clouds or between patchy clouds. For every grid cell, we precompute whether straight paths to the detector are cloud- and aerosol-free from all cell corners as well as for several points within each cell. If these paths pass through gas only, the grid cell is flagged. Assuming that the gas is horizontally homogeneously distributed, we use Eq. 15 for events in the flagged cells, eliminating the need for photon propagations between the event locations and the detector. This approach is computationally more efficient compared to evaluating Eq. 9, while its results are identical.

2.5 Simulation rounds and noise estimation

The computation of the TOA reflectance or BOA transmittance with Eq. 14 and N photons represents one simulation round. In practice, we perform N_r independent simulation rounds. As an example, consider the simulation of the TOA reflectance R_r estimated with N photons as in Eq. 14 (we have omitted the notation of the matrix element indices for readability and introduced the subscript r indicating the simulation round number). The final result that we report is the mean TOA reflectance estimated from all simulation rounds:

$$\overline{R} = \frac{\sum_{r=1}^{N_r} R_r}{N_r}, \tag{16}$$

https://doi.org/10.5194/egusphere-2025-2197
Preprint. Discussion started: 14 July 2025

We compute the noise as the standard deviation of the mean (see Eq. 4.46 of Marshak and Davis, 2005):

$$\sigma_{\overline{R}} = \sqrt{\frac{1}{N_r - 1}\left[\frac{1}{N_r}\sum_{r=1}^{N_r} R_r^2 - \left(\frac{\sum_{r=1}^{N_r} R_r}{N_r}\right)^2\right]}. \tag{17}$$

To ensure a reliable estimate of $\sigma_{\overline{R}}$, we impose that $N_r \geq 30$.

2.6 Backward Monte Carlo simulation

MONKI can be used both in the forward and in the backward mode, where photon paths are traced from the detector to the light source. The backward mode is significantly more efficient than the forward mode in case the detector is at a finite distance from the atmosphere–surface system. The reason is that in forward mode, only a small fraction of the photons from the source end up in the detector's field of view. In the backward mode, every photon that is not completely absorbed contributes to the result, assuming that the light source is at an infinite distance.

According to the reciprocity principle (see Sect. 2.4 of Hovenier et al., 2004), reversing a light path through a medium preserves the reflectance and transmittance along the original path. In practice, this principle allows swapping the light source and detector in a radiative transfer simulation: $\theta \to \theta_0$, $\theta_0 \to \theta$, $\varphi \to \varphi_0 + 180°$, and $\varphi_0 \to \varphi + 180°$. To compute the TOA reflectance in backward mode, photons are injected downward into the domain at TOA along the reversed viewing direction. For the BOA transmittance, photons are injected upward from the surface, also along the reversed viewing direction.

Because MONKI accounts for polarisation, the orientation of the Stokes vector must be mirrored relative to the reference plane when tracing the reversed photon trajectory. Consequently, in the backward mode, the $\boldsymbol{\chi}$ matrices must be modified as follows (see Eq. 3.37 of Hovenier et al., 2004)[4]:

$$\boldsymbol{\chi}_{\mathrm{bw}}(-\mu, -\mu_0, \varphi_0 - \varphi) = \boldsymbol{\Delta}_3 \boldsymbol{\chi}^T(\mu, \mu_0, \varphi - \varphi_0)\boldsymbol{\Delta}_3, \tag{18}$$

with $\boldsymbol{\chi}^T$ the transpose of $\boldsymbol{\chi}$ and with $\boldsymbol{\Delta}_3$ given by

$$\boldsymbol{\Delta}_3 = \begin{pmatrix} 1 & 0 & 0 & 0 \\ 0 & 1 & 0 & 0 \\ 0 & 0 & -1 & 0 \\ 0 & 0 & 0 & 1 \end{pmatrix}. \tag{19}$$

Finally, in the backward mode, the incident Stokes vector $\boldsymbol{I}_0 = [1,0,0,0]^T$ must be multiplied by the $\boldsymbol{\chi}$ matrices at the end of the photon trajectory. That is, the event's contribution to the TOA reflectance or the BOA transmittance is computed as follows:

$$\boldsymbol{\Phi}_{\mathrm{bw}} = w \cdot \overline{\boldsymbol{W}} \cdot \boldsymbol{\chi}_{\mathrm{bw}} \cdot \boldsymbol{I}_0 \cdot \exp\left(-\int_0^{s_{\mathrm{sun}}} \beta(s')ds'\right), \tag{20}$$

[4]The relation of Eq. 18 is only valid for particles very small compared to the wavelength, or particles accompanied by their mirror particles in equal numbers and in random orientation, or particles with a plane of symmetry (such as spheres, spheroids, ellipsoids, cylinders and cubes) that are randomly oriented (see Hovenier et al., 2004, Sects. 2.4, 2.7 and 3.3).

https://doi.org/10.5194/egusphere-2025-2197
Preprint. Discussion started: 14 July 2025

where the direct transmittance is calculated from the event location ($s = 0$) to the light source ($s = s_{\text{sun}}$). Here, $\overline{\boldsymbol{W}}$ is the 4 × 4 normalised 'weight matrix', which starts as the identity matrix at the beginning of the simulation. It is updated at each event to account for the continuation of the photon's trajectory in the new direction (ϑ, φ), as follows:

$$\boldsymbol{W} = \overline{\boldsymbol{W}} \cdot \boldsymbol{\chi}_{\text{bw}}(\vartheta, \varphi), \tag{21}$$

after which it is normalised by its upper left element: $\overline{\boldsymbol{W}} = \boldsymbol{W}/W_{11}$. Note that the right-multiplications by $\boldsymbol{\chi}_{\text{bw}}$ in Eq. 21 for all scattering (and reflection) events are applied before the multiplication by $\boldsymbol{I}_0$ in Eq. 20 (see also Collins et al., 1972).

3 Validation results

In this section, we present the validation of MONKI. In Sect. 3.1, we validate MONKI's total and polarised radiances for horizontally homogeneous scenes by comparing them with results from the widely used doubling–adding method. In Sect. 3.2, we validate MONKI's total and polarised radiances against benchmark results for thick Rayleigh-scattering atmospheres. In Sect. 3.3, we validate MONKI for scenes with 3D cloud structures.

3.1 Comparison with de Haan et al. (1987)

Here, we present a comparison of total and polarised radiances that emerge from a horizontally homogeneous atmosphere (i.e., $N_x = N_y = 1$) with the benchmark results of de Haan et al. (1987), who used an efficient doubling-adding algorithm that included full polarisation for all orders of scattering.

The paper by de Haan et al. (1987) lists benchmark results for different atmosphere-surface systems. We compare with their results for an atmosphere with a total optical thickness $b = 0.6$, that consists of two plane-parallel layers. Both layers contain gaseous molecules with a scattering optical thickness $b^{\text{m}}_{\text{sca}} = 0.1$. The bottom layer also contains water-haze L aerosols (Deirmendjian, 1969), with a scattering optical thickness $b^{\text{c}}_{\text{sca}} = 0.4$. The aerosol characteristics and expansion coefficients at $\lambda = 0.70$ μm are provided by de Rooij and van der Stap (1984). There is no absorption of light ($b^{\text{m}}_{\text{abs}} = b^{\text{c}}_{\text{abs}} = 0$), and the depolarisation factor of the gaseous molecules is 0.0279, a typical value for terrestrial air. The atmosphere is illuminated from above by unidirectional, unpolarised light propagating in the direction $(\mu_0,\ \varphi_0) = (0.5,\ 0°)$ with a total flux E_0 equal to π. The Lambertian reflecting surface has an albedo A_{s} of 0.1.

Table 1 shows the results of both codes for the radiances at TOA for six viewing geometries: $\mu = \{0.1,\ 0.5,\ 1.0\}$ and $\varphi = \{0°,\ 30°\}$ (see Table 9 of de Haan et al., 1987). The MONKI simulations used 10^7 photons. The listed errors represent twice the standard deviation of the results, computed using Eq. 17. The results agree excellently: almost all differences between the MONKI results and those of de Haan et al. (1987) fall within the two standard deviations. The magnitude of these differences is comparable to that reported by MYSTIC for simulations with 10^7 photons, as shown in Table 2 of Emde et al. (2010). The MONKI results for a solar geometry with $(\mu_0,\ \varphi_0) = (0.1,\ 0)$ and those for an observer on the surface (not in Table 1) show excellent agreement, too (see Tables S1, S2, and S3).

https://doi.org/10.5194/egusphere-2025-2197
Preprint. Discussion started: 14 July 2025

Table 1. Comparison of the TOA radiances computed using MONKI with the benchmark results of de Haan et al. (1987) for an atmosphere consisting of two plane-parallel layers with a total optical thickness $b = 0.6$ (see text). The direction of the incident unpolarised light beam is $(\mu_0,\ \varphi_0) = (0.5,\ 0.0)$. The reported uncertainties in the MONKI results refer to two times the standard deviation (Eq. 17).

		$\mu = 0.1$		$\mu = 0.5$		$\mu = 1.0$	
		de Haan	MONKI	de Haan	MONKI	de Haan	MONKI
$\mu_0 = 0.5$	I	0.532950	0.532769±0.000534	0.208430	0.208518±0.000239	0.093680	0.093687±0.000071
$\varphi = 0°$	Q	-0.028340	-0.028364±0.000136	-0.036299	-0.036339±0.000067	-0.024156	-0.024169±0.000037
	U	0.000000	0.000027±0.000119	0.000000	-0.000030±0.000046	0.000000	0.000002±0.000024
	V	0.000000	-0.000008±0.000010	0.000000	0.000001±0.000006	0.000000	0.000000±0.000002
$\mu_0 = 0.5$	I	0.418140	0.418068±0.000427	0.184970	0.185032±0.000217	0.093680	0.093687±0.000071
$\varphi = 30°$	Q	-0.000058	-0.000068±0.000137	-0.019649	-0.019667±0.000061	-0.012078	-0.012086±0.000027
	U	-0.073705	-0.073132±0.000162	-0.041401	-0.041454±0.000080	-0.020920	-0.020930±0.000035
	V	0.000106	0.000111±0.000012	0.000040	0.000047±0.000006	0.000000	0.000000±0.000002

3.2 Comparison with Natraj and Hovenier (2012)

The model atmospheres used by de Haan et al. (1987) are optically relatively thin. Here, we compare with the benchmark results of Natraj and Hovenier (2012), who reported total and polarised radiances of light that is reflected and transmitted by optically thick Rayleigh-scattering atmospheres, computed using the method of X and Y functions (Chandrasekhar, 1960; Natraj et al., 2009). According to Natraj and Hovenier (2012), their results are accurate up to eight decimal places.

We compare to their Tables 1, 3, and 5, which list the Stokes parameters I, Q and U of light that is reflected by a homogeneous atmospheric layer with an optical thickness of $b = 16$. The layer contains only gas, which does not absorb and which has a depolarisation factor of zero. The surface below the layer is black. The atmosphere is illuminated from the top by a beam of unpolarised light with $E_0 = \pi$, with directions $\mu_0 = 0.2$ and $\varphi_0 = 0°$. Under these conditions, no circularly polarised light will emerge, thus $V = 0$ (it is not included in the tables). Figure 3 shows Stokes parameters I, Q and U computed by MONKI in forward mode using 10^8 photons, and as listed by Natraj and Hovenier (2012). Viewing direction μ ranges from 0 to 1.0 (nadir viewing direction), and φ from 0° to 180°. As can be seen, the agreement between the results of MONKI and those of Natraj and Hovenier (2012) is excellent for all geometries. Indeed, the maximum differences in I, Q, and U are 1.2×10^{-4}, 5.4×10^{-5}, and 5.3×10^{-5}, respectively. They fall within the 2 standard deviation noise values for I, Q, and U: 1.6×10^{-4}, 8.0×10^{-5}, 5.6×10^{-5}, respectively. Additionally, our numerical tests show that the differences decrease further when increasing the number of photons.

https://doi.org/10.5194/egusphere-2025-2197
Preprint. Discussion started: 14 July 2025

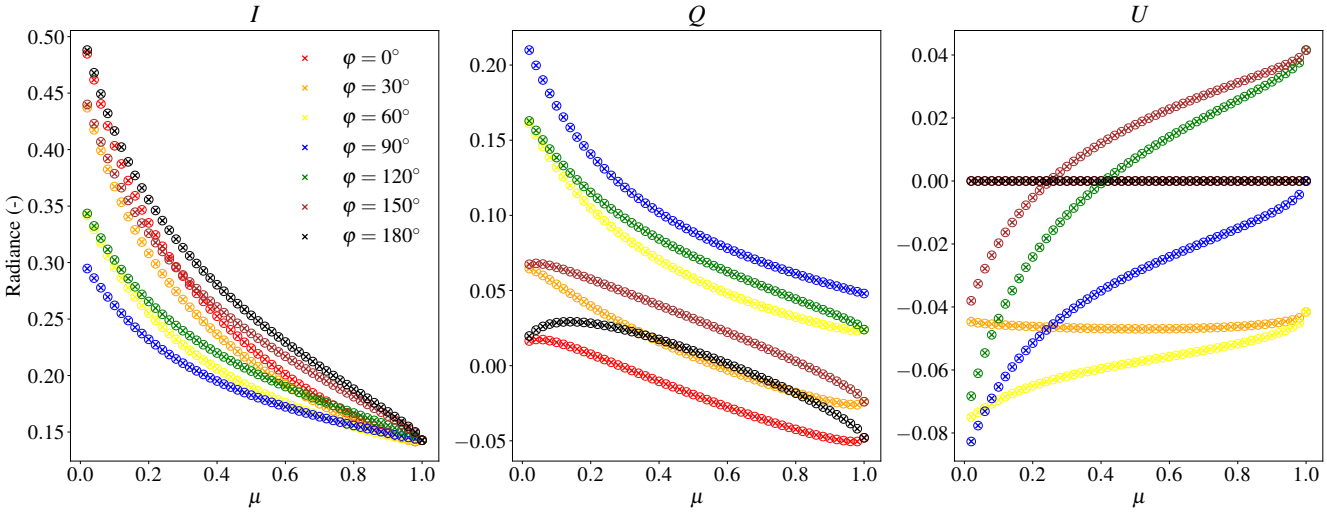

Figure 3. Comparison of the TOA radiances I, Q and U computed with MONKI (crosses) with the benchmark results from Natraj and Hovenier (2012) (circles), for a Rayleigh-scattering atmosphere with an optical thickness $b = 16$, a single scattering albedo of 1.0, a depolarisation factor of 0.0, and a black surface below. The colours indicate different values of φ ($\varphi_0 = 0°$).

Note that García Muñoz and Mills (2015) wrote that for thick, strongly polarising[5] atmospheres, such as those used by Natraj and Hovenier (2012), some Monte Carlo codes may fail to converge. For examples of such codes, García Muñoz and Mills (2015) referred to MYSTIC (Emde et al., 2010) and the integral-vector Monte Carlo method (IVMCM) (Gay et al., 2010). As shown by García Muñoz and Mills (2015) (in their Fig. 8), the non-convergence arises from neglecting the polarisation state of the incident photon when sampling a new scattering direction, and by then correcting for the neglect by adjusting the photon's weighting factor (see, e.g., Collins et al., 1972; Emde et al., 2010).

In optically thick atmospheres where photons are on average scattered multiple times, this correction procedure leads to a significantly poorer sampling of certain scattering directions.

MONKI fully accounts for the photon's polarisation history and thus does not include such corrections (see Appendices D, E, and F), and MONKI indeed converges for thick Rayleigh-scattering atmospheres in both its forward and backward mode. Figure 4 shows MONKI's convergence when computing the TOA reflectance R_{11} in both the forward and the backward mode, for photon numbers up to 10^7, for $\mu = 1.0$, $\varphi = 0°$, and $\varphi_0 = 0°$, different solar angles μ_0, and different optical thicknesses b (the single scattering albedo is 1.0). The surface is black.

The lines in Fig. 4 clearly show MONKI's convergence with increasing photon numbers. Indeed, for $\mu = 1.0$ with $b = 16$ and with $b = 4$, the lines pertaining to MONKI's forward and the backward mode are virtually the same (those cases were also used by García Muñoz and Mills (2015) to demonstrate non-convergence when one corrects for the negligence of polarisation, see their Fig. 8). This was also to be expected, as for this solar and viewing geometry ($\mu = \mu_0$), the photon paths in the forward

[5]Note that for such atmospheres, the radiation that is observed emerging at TOA or BOA will generally have a low degree of polarisation because it comprises light with a broad range of polarisation states.

https://doi.org/10.5194/egusphere-2025-2197
Preprint. Discussion started: 14 July 2025

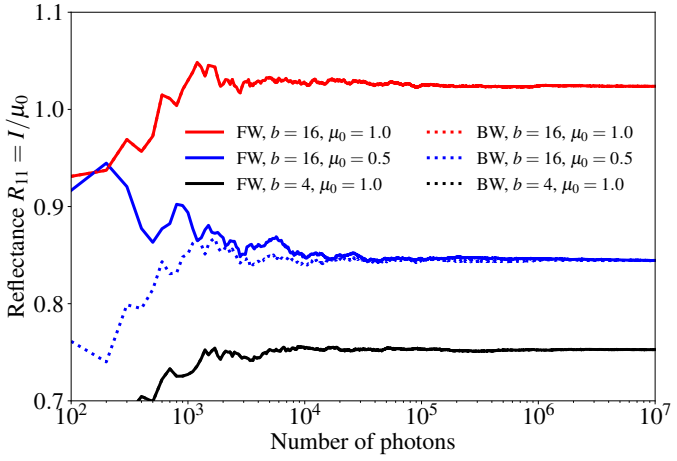

Figure 4. Convergence history of the TOA reflectance, R_{11}, by MONKI in forward mode (solid lines) and backward mode (dotted lines) for a Rayleigh scattering atmosphere with $b = 4$ and $\mu_0 = 1.0$ (black), $b = 16$ and $\mu_0 = 0.5$ (blue), and $b = 16$ and $\mu_0 = 1.0$ (red). The viewing zenith angle $\mu = 1.0$. For $\mu_0 = 1.0$, the dashed and dotted lines overlap.

and backward direction are identical. For $\mu = 1.0$ and $\mu_0 = 0.5$, the photon paths in the forward mode differ from those in the backward mode, and consequently, although MONKI converges to the same values, its convergence history is different for the forward and backward modes. These results demonstrate the convergence of MONKI for optically thick atmospheres.

3.3 Comparison with Emde et al. (2018)

In the previous sections, we validated MONKI for horizontally homogeneous atmosphere-surface systems. Here, we validate MONKI for horizontally inhomogeneous (3D) cloudy atmospheres by comparing MONKI's results with benchmarks from the polarised radiative transfer model intercomparison project (IPRT) (Emde et al., 2018).

Our first comparison with results from the IPRT is for a homogeneous Rayleigh scattering atmosphere with $b = 0.5$, that has a cubic-shaped cloud with an optical thickness of 10 embedded (see Sect. 5 of Emde et al., 2018). The single scattering albedo of the gaseous molecules is 1.0 and the depolarisation factor is set to 0.0. The cloud droplets are spherical with effective radii of 10 μm, and have a gamma size distribution with an effective variance of 0.1. Their single scattering albedo is 1.0. We use their single scattering matrices at $\lambda = 800$ nm as provided by the IPRT. The surface reflects Lambertian with an albedo of 0.2.

The cloud has dimensions of $1\times1\times1$ km^3, and extends from 2 to 3 km altitude. The computational domain extends to an altitude of 5 km. Horizontally, the domain spans 7 km in both directions, with periodic boundary conditions. Both the light source and the detector are at infinite distances from the atmosphere-surface system: the solar and viewing geometries are the same across the domain. The horizontal area of 7×7 km^2 is covered by 70×70 pixels. MONKI used 10^7 photons per pixel, matching the number of photons used in the IPRT (Emde et al., 2018).

Figure 5 shows the results of MONKI (in forward mode) for the radiance I and degree of polarisation P, for IPRT-cases 4 and 9, that differ in solar and viewing geometries (see Table 4 of Emde et al., 2018). Because MONKI defines the angles

https://doi.org/10.5194/egusphere-2025-2197
Preprint. Discussion started: 14 July 2025

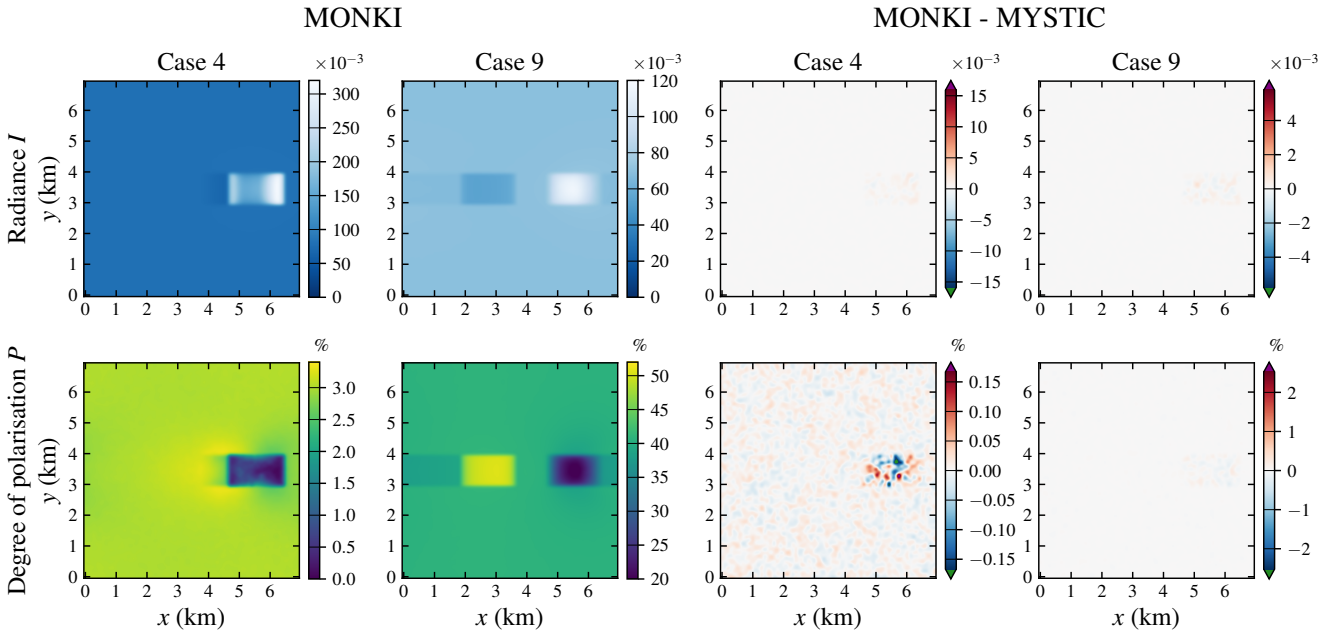

Figure 5. MONKI results (columns 1 and 2) of the radiance I divided by E_0 (top row) and degree of polarisation P in % (bottom row), for a cubic cloud inside a Rayleigh scattering atmosphere, and the differences between the MONKI results and those of MYSTIC (columns 3 and 4). Results are shown for 2 of the 9 cases described by Emde et al. (2018). In case 4 (columns 1 and 3), the detector is on the surface (BOA), and in case 9 (columns 2 and 4), the detector is at TOA. The sunlight is incident from left to right along the x-direction. The solar and viewing angles are given in Table S4. Because of the horizontal periodicity, the cloud shadow crosses the right domain boundary and re-enters the domain on the left hand side.

slightly different from Emde et al. (2018), we have listed the geometries in Table S4 in the Supplementary Material. Figure S1 in the Supplementary Material shows the results for all 9 cases and all Stokes parameters, with cases 1 to 4 pertaining to light transmitted through the atmosphere, thus at BOA, and cases 5 to 9 pertaining to reflected light, thus at TOA. Results for cases 1 to 4 are stored on the x, y-grid at the surface, whereas results for cases 5 to 9 are stored on the x, y-grid at TOA.[6]

The radiance I in the cloud-free regions of cases 1 to 4 (BOA) is smaller than in cases 5 to 9 (TOA), due to the larger contribution of the surface reflection in the latter cases (see Fig. S1). Cases 5 to 9 (TOA) show shadows on the surface, while cases 1 to 4 (BOA) only show subtle shadows in the sky. Note that due to horizontal periodicity, the shadow of the cloud stretches outside the right hand side of the domain and back into the domain on the left hand side. The difference between the surface and sky shadows are, for instance, evident in P for case 9 (see Fig. 5), where P to the right of the cloud is relatively low due to the atmospheric shadow: in this part of the atmosphere, the direct sunlight is attenuated by the cloud. Instead, this part of the atmosphere is mostly illuminated by diffuse light with generally a lower degree of polarisation due to randomisation (see

[6]MONKI can also map the reflected light at TOA on the x, y-grid at the surface, making MONKI suitable for air- and spaceborne applications which typically store measurements on ground-based pixel grids.

https://doi.org/10.5194/egusphere-2025-2197
Preprint. Discussion started: 14 July 2025

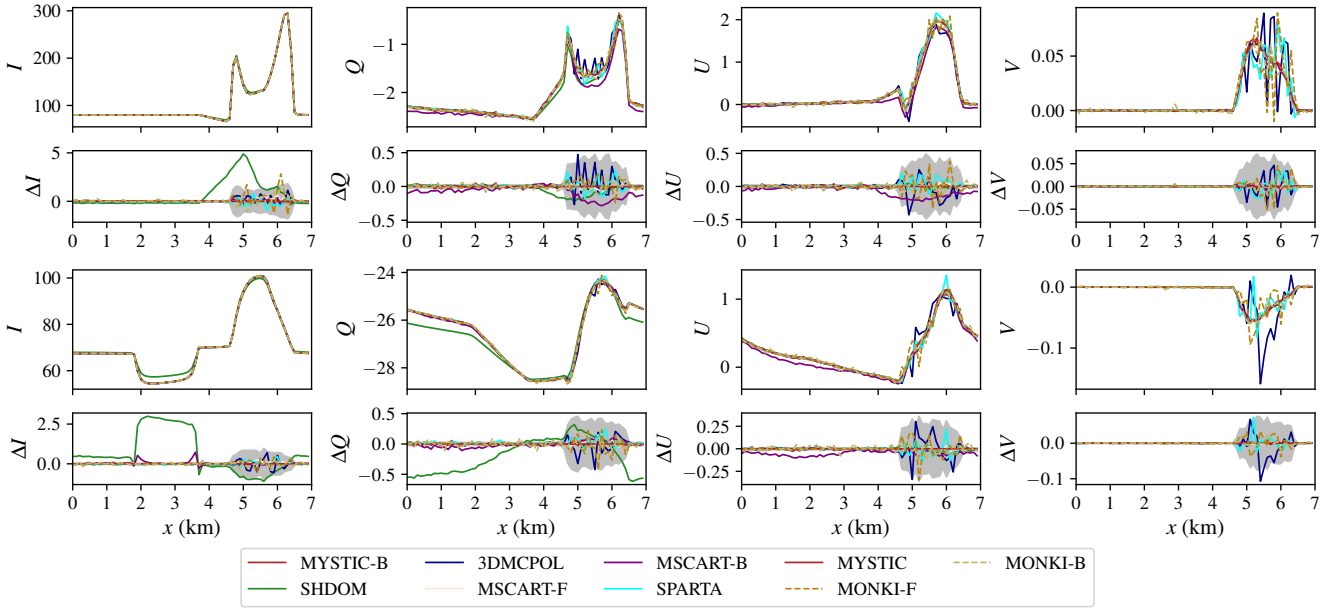

Figure 6. Results of MONKI in forward ('MONKI-F') and backward mode ('MONKI-B') for the cubic cloud scenario of Emde et al. (2018), cases 4 (rows 1 and 2) and 9 (rows 3 and 4), for a cross-section through the domain at $y = 3.95$ km (see Fig. 5). Stokes parameters I, Q, U and V are shown in four columns, also for the other codes in the IPRT project, with the absolute differences of all codes with MYSTIC below. The grey area in the difference plots corresponds to 2 standard deviations of 3DMCPOL. The Stokes parameters are divided by $1000/E_0$.

Fig. 7 of Trees et al., 2025). Above the cloud shadow on the surface, P is high because the shadow suppresses the unpolarised contribution of light that has been reflected by the Lambertian surface. For a detailed discussion of the features in Figs. 5 and S1, see Sect. 5 of Emde et al. (2018).

MONKI's results closely match the benchmark results (cf. Fig. A2 of Emde et al., 2018). Figure 5 shows the differences between MONKI and MYSTIC for test cases 4 and 9 for I and P, and Fig. S2 in the Supplementary Material shows the differences for all nine cases and all Stokes parameters. In the cloud-free regions, the differences in I, Q, U, and V are nearly zero. Small, random differences in P remain below 0.07% and are centred around zero. In cloudy pixels, the differences are larger, as expected because of increased simulation noise. This effect is common in Monte Carlo codes due to infrequent but significant contributions in the local estimation method associated with strongly forward-peaked Mie scattering phase functions of the cloud droplets (see, e.g., Barker et al., 2003). Nevertheless, these differences remain below 2.82×10^{-3}, 0.66×10^{-3}, 0.63×10^{-3}, 10.98×10^{-5}, and 0.49 % for I, Q, U, V, and P, respectively, and are centred around zero for all cases. Increasing the number of photons would reduce this random noise. We find no systematic biases between MONKI and MYSTIC.

To demonstrate how MONKI performs compared to other codes, Fig. 6 shows cross-sections of the results of cases 4 and 9 at $y = 3.95$ km in Fig. 6, of MONKI in both forward and backward mode, together with results of the codes used in the

https://doi.org/10.5194/egusphere-2025-2197
Preprint. Discussion started: 14 July 2025

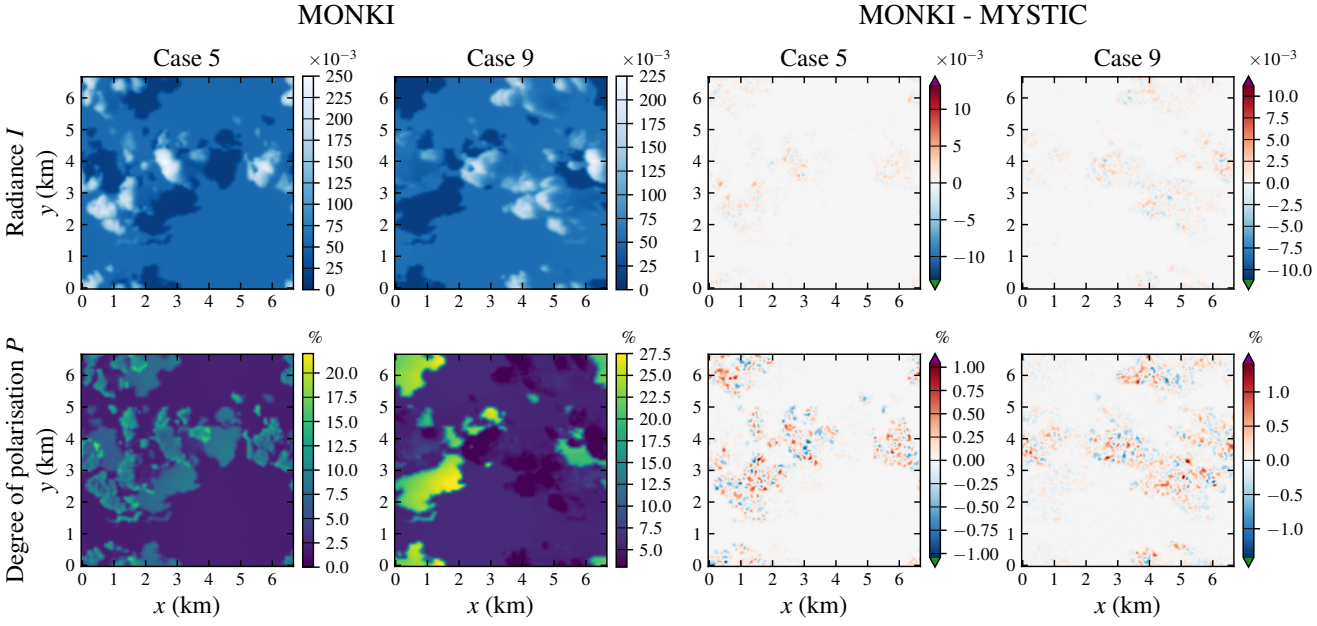

Figure 7. MONKI results (columns 1 and 2) of the radiance I (row 1) and P (row 2), for a 3D cumulus cloud field inside a scattering and absorbing gaseous atmosphere (Emde et al., 2018), for 2 different solar and viewing geometries with an observer at TOA (cases 5 and 9 in Table S4). The sunlight is incident from left to right along the x-direction. Radiance I is divided by E_0, and P is in %. Columns 3 and 4 show the differences between MONKI and MYSTIC.

IPRT-project (Emde et al., 2018). Also, the differences with MYSTIC are shown, on top of the 2 standard deviation of the results of 3DMCPOL. The results for all nine cases are shown in Fig. S5 in the Supplementary Material. Unlike some other codes, MONKI shows excellent agreement with MYSTIC in all cases, in both its forward and backward mode.

Emde et al. (2018) also provide test cases for a more realistic scenario: a 3D cumulus cloud field that has been generated by a Large Eddy Simulation (LES) code (Stevens et al., 1999), embedded within a scattering and absorbing gaseous atmosphere. The domain size is $6.7 \times 6.7 \times 30\,\mathrm{km}^3$. The cloud's optical thickness and droplet effective radius vary across the $100 \times 100 \times 53$ grid cells (the 12 top layers are cloud-free). For a detailed description of the model, see Emde et al. (2018). Figure 7 shows I and P as computed with MONKI for the solar and viewing geometries of cases 5 and 9 (see Table S4), along with their differences from MYSTIC benchmark results. We used 10^6 photons per pixel. Once again, we find no systematic biases. Numerical tests showed that the remaining differences decrease when increasing the number of photons.

4 Sample signals for the Earth and Venus

In this section, we present sample simulations with MONKI of sunlight that is locally reflected by the atmospheres of the Earth and Venus. The model atmospheres were horizontally homogeneous (i.e., $N_x = N_y = 1$), as illustrated in Fig. 8. These

https://doi.org/10.5194/egusphere-2025-2197
Preprint. Discussion started: 14 July 2025

Table 2. Model settings used in the sample simulations of the Earth and Venus at $\lambda = 550$ nm.

Setting	Earth	Venus
Altitude range	0–100 km (33 layers)	0–100 km (40 layers)
Surface albedo A_s	0.05	0.0
Vertical temperature-pressure profile	MLS	VIRA
Gravitational acceleration g	9.81 m s^{-2} (not used)	8.87 m s^{-2}
Real refractive index n of the gas	Peck and Reeder (1972)	Wilmouth and Sayres (2020)
Depolarisation factor δ	0.0283 for air	0.0789 for CO_2
Absorbing gases	O_3 (MLS profile)	None
Absorption cross-sections $\sigma_{\mathrm{abs}}^{\mathrm{m}}$	Bass and Paur (1985)	—
Cloud altitude range	1–2 km	50–70 km
Cloud optical thickness b^{c}	5	30
Cloud particle type	Liquid water	Liquid 75% H_2SO_4 solution
Particle size distribution	Two-parameter gamma	Two-parameter gamma
Effective radius r_{eff}	10 μm	1.05 μm
Effective variance v_{eff}	0.1	0.07
Real refractive index of the liquid droplets	1.33	1.43
Imaginary refractive index of the liquid droplets	0	0

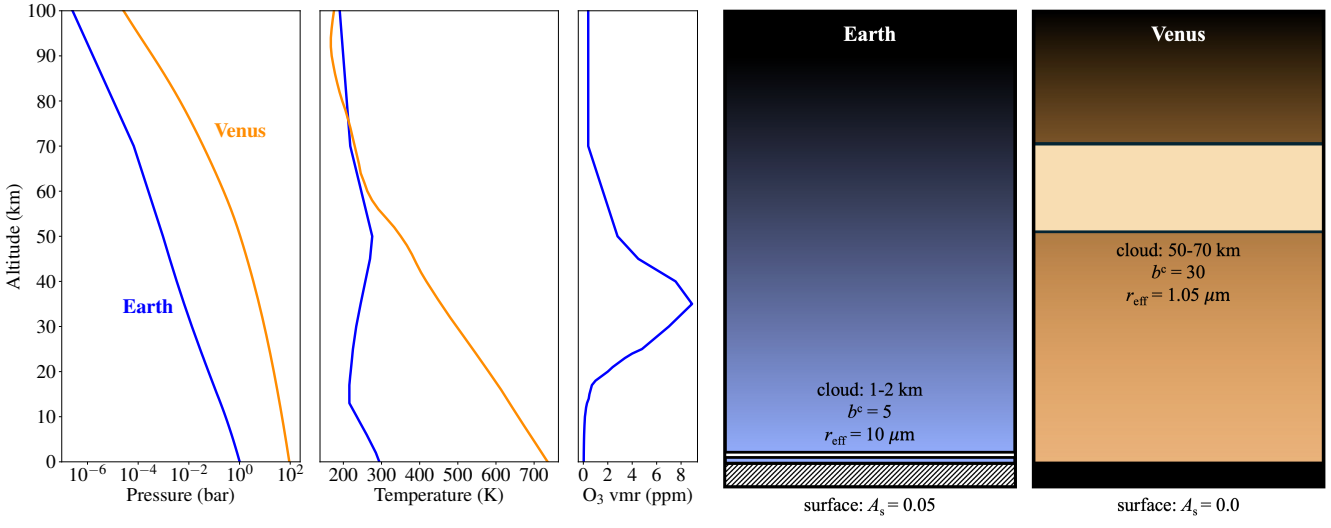

Figure 8. The model atmosphere-surface systems of the Earth (in blue) and Venus (in orange). From left to right: the pressure profiles, temperature profiles, the ozone volume mixing ratio profile for the Earth, the cloud model for the Earth, the cloud model for Venus. Below the latter two graphs, the surface albedo, A_s, is also given.

https://doi.org/10.5194/egusphere-2025-2197
Preprint. Discussion started: 14 July 2025

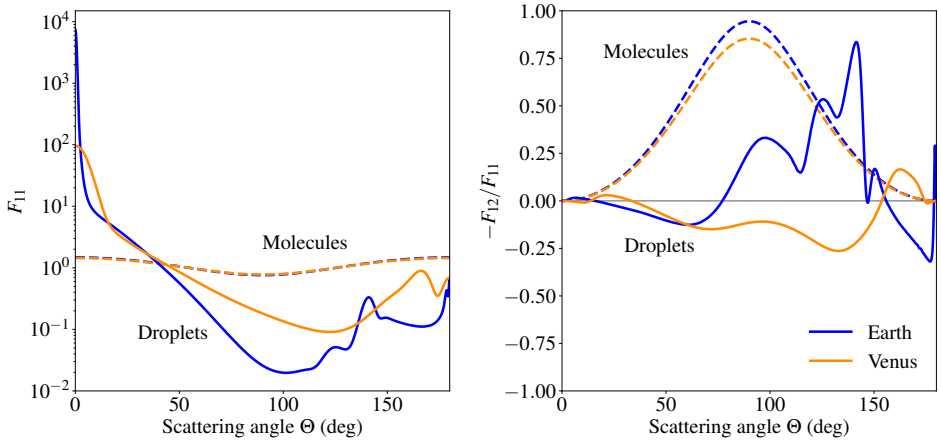

Figure 9. The phase function F_{11} (left) and the degree of linear polarisation ($-F_{12}/F_{11}$) (right) as functions of the scattering angle Θ, for light that is singly scattered by gaseous molecules (dashed lines) or cloud droplets (solid lines). The blue lines are for Earth-like gas (with a depolarisation factor δ equal to 0.0283) and cloud particles (with an effective droplet radius of 10 μm), and the orange lines are for Venus-like gas (with $\delta = 0.0789$) and cloud particles (with an effective droplet radius of 1.05 μm). The wavelength of the light is 550 nm.

simulations demonstrate MONKI's versatility in handling different types of atmospheres, following the formulae provided in Appendix A. Below, we first describe the model setting and then the results. The model settings are also summarized in Tab. 2.

The atmosphere of the Earth's model consists of 33 plane-parallel, horizontally homogeneous layers from 0 to 100 km altitude. The surface reflects Lambertian with an albedo A_s of 0.05. The only absorbing gas is ozone (O_3). The wavelength- and temperature-dependent O_3 absorption cross-sections, $\sigma^{\rm m}_{\rm abs}(\lambda, T)$, are taken from Bass and Paur (1985). Pressure, temperature, and ozone volume mixing ratios (VMRs) vary with altitude according to the standard Mid-Latitude Summer profile (Anderson et al., 1986). We assume that the pressure-to-temperature ratio decreases exponentially with altitude within each layer (see Eq. A10). The refractive index of air, n, is computed with the dispersion formula of Peck and Reeder (1972). The King correction factor $F_{\rm K}$ of the air (Eq. A9) is the sum of the values for N_2, O_2, Ar, and CO_2 as given by Bates (1984), weighted by the respective mixing ratios of those gases on Earth: 78.084%, 20.9476%, 0.934%, and 0.0375%. At $\lambda = 550$ nm, this yields a depolarisation factor $\delta = 0.0283$.

The Earth scenario cloud extends from 1 to 2 km, with a vertically homogeneous optical thickness $b^{\rm c}$ of 5. We assume a two-parameter gamma distribution for cloud droplet sizes (Hansen and Travis, 1974), with an effective radius $r_{\rm eff} = 10$ μm and an effective variance $v_{\rm eff} = 0.1$. The droplets are composed of liquid water with a real refractive index of 1.33 (Hale and Querry, 1973) and an imaginary refractive index of zero (i.e., the single scattering albedo of the cloud droplets is 1.0).

The Venus model atmosphere consists of 40 plane-parallel, horizontally homogeneous layers from 0 to 100 km altitude. At $\lambda = 550$ nm, the reflected light at TOA is virtually insensitive to Venus's lower atmosphere and surface albedo. Therefore, we use 4 km thick layers from the surface to 40 km and 2 km thick layers above 40 km. The surface is assumed black. We neglect gaseous absorption, which is a reasonable assumption for Venus at $\lambda = 550$ nm (Moroz, 1981; Haus et al., 2015). Pressure profiles follow the Venus International Reference Atmosphere (VIRA) for latitudes up to 30°, based on Seiff et al. (1985), which incorporates data from four Pioneer Venus Probes, the Pioneer Venus Orbiter, and the Venera 10, 12, and 13 landers. We

https://doi.org/10.5194/egusphere-2025-2197
Preprint. Discussion started: 14 July 2025

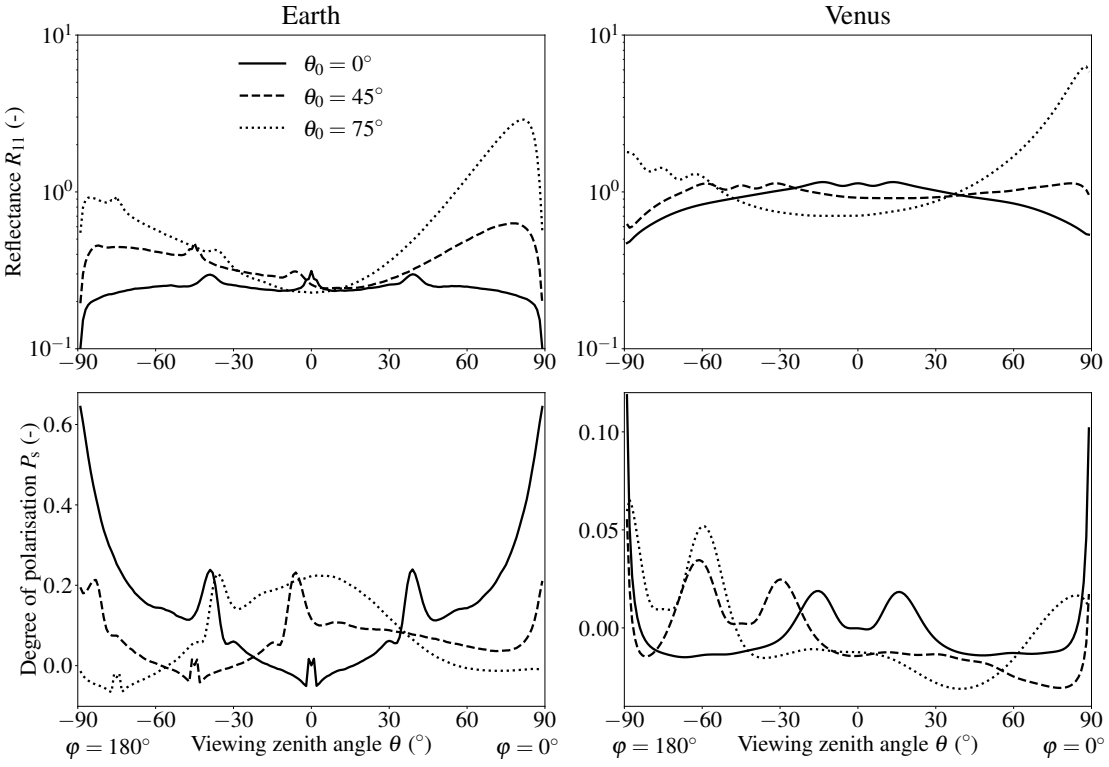

Figure 10. Sample signals of the TOA reflectance R_{11} (top) and degree of polarisation $P_s = -Q/I$ (bottom), for the Earth (left) and Venus (right), computed with MONKI. Note the different y-scales for P_s. The signals are presented as functions of viewing angle θ, and for solar zenith angles $\theta_0 = 0°$ (solid line), $45°$ (dashed line), and $75°$ (dotted line). The solar azimuth angle φ_0 is $0°$.

assume hydrostatic equilibrium (Eq. A11), a gravitational acceleration of $g = 8.87$ m s^{-2}, and the background gas molecular mass M is computed by the weighted sum of 96.5% CO_2 (44.01 g mol^{-1}) and 3.5% N_2 (28.0134 g mol^{-1}). The values for n and F_K at $\lambda = 550$ nm are computed with the parametrisations for CO_2 stated in Sneep and Ubachs (2005)[7], leading to a depolarisation factor $\delta = 0.0789$.

The cloud in the Venus model extends from 50 to 70 km, with a vertically homogeneous optical thickness $b^c = 30$. The cloud particles are liquid droplets and their properties follow those of Hansen and Hovenier (1974): a two-parameter gamma distribution with an effective radius of 1.05 μm and an effective variance of 0.07. The droplets are composed of 75% H_2SO_4 solution in water, with a real refractive index of 1.43 at $\lambda = 550$ nm (Palmer and Williams, 1975). Their single scattering albedo is 1.0.

Figure 9 shows the singly scattered radiance, F_{11} (the phase function), and the degree of linear polarisation, $-F_{12}/F_{11}$, of the gas and cloud droplets in the Earth and Venus model atmospheres as functions of the scattering angle Θ (see App. A for definitions of the single-scattering matrix elements). The large droplets of the Earth cloud produce a strong forward peak

[7]The refractive index of CO_2 stated in Sneep and Ubachs (2005) needs to be divided by 10^3, see Wilmouth and Sayres (2020).

https://doi.org/10.5194/egusphere-2025-2197
Preprint. Discussion started: 14 July 2025

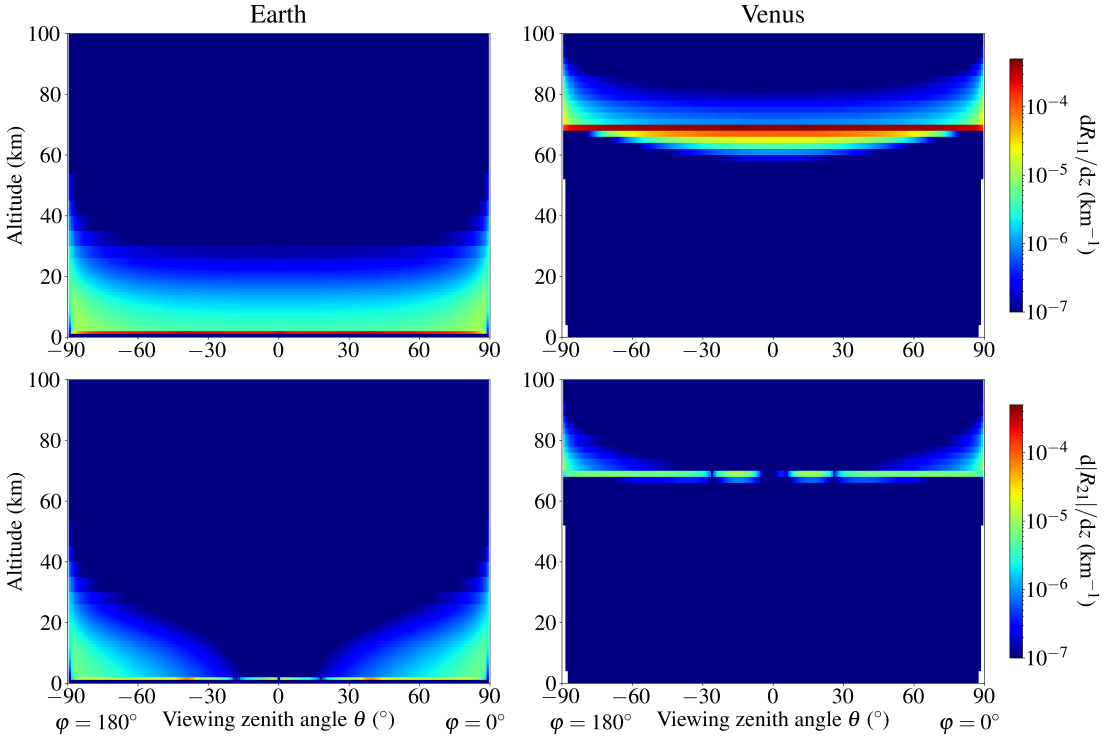

Figure 11. Contributions to the computed TOA reflectances at $\theta_0 = 0°$, for Earth (left) and Venus (right), plotted at the altitudes of the last scattering event of the photons (in km^{-1}), for the total reflectances R_{11} (top row) and the polarised reflectances $|R_{21}|$ (bottom row).

in F_{11} due to diffraction (see Hansen and Travis, 1974). The peaks near $\Theta = 142°$ and $122°$, are the primary and secondary cloudbows, caused by, respectively, one and two internal reflections inside the spherical droplets. The radiance and polarisation enhancement near $\Theta = 180°$ is called the 'glory'. These features are less pronounced or absent in the much smaller cloud droplets on Venus. The features due to Rayleigh scattering by gas molecules are similar on Earth and Venus: F_{11} is stronger in the forward and backward directions, while polarisation is strongest around $\Theta = 90°$. For the Venusian gas, the Rayleigh polarisation maximum is lower than for the Earth's gas because it has a larger depolarisation factor.

Figure 10 shows the simulated TOA reflectance, R_{11}, and degree of polarisation, P_s, computed with MONKI for the Earth and Venus model atmosphere–surface systems described above. Simulations were performed for three solar zenith angles: $\theta_0 = 0°$, $45°$, and $75°$. The viewing zenith angles range from $\theta = 0°$ to $\theta = 89°$ in $1°$ increments. The solar azimuth angle is $\varphi_0 = 0°$. The viewing azimuth angles are $\varphi = 0°$ and $180°$. For each combination of the 90 values of θ, and (θ_0, φ), we used 10^8 photons for the computations for the Earth and 10^5 photons for Venus (the more isotropic scattering by the small Venusian cloud droplets requires fewer photons). In Fig. S6, we provide the comparison of the computations for the Earth with results computed with Doubling-Adding KNMI (DAK), which uses identical formulae for the optical properties of the model atmosphere as MONKI (see Appendix A).

https://doi.org/10.5194/egusphere-2025-2197
Preprint. Discussion started: 14 July 2025

For the Earth model (Fig. 10), the reflectance R_{11} generally increases with θ and θ_0. With increasing angles, the optical paths through the gas and clouds increase and multiple scattering increases. Cloud droplet single scattering features (Fig. 9) leave signatures in R_{11}, but show up more distinctly in P_s. The cloudbows emerge near (θ,φ) = $(38°,0°)$, $(7°,180°)$, and $(37°,180°)$, corresponding to the single scattering angle $\Theta = 142°$ for $\theta_0 = 0°$, $45°$ and $75°$, respectively.[8] The glory shifts from $\theta = 0°$ to $45°$ to $75°$ in the $\varphi = 180°$ direction with increasing θ_0. Rayleigh scattering, which enhances P_s around $\Theta = 90°$, causes P_s to peak near $\theta = 90°$ for $\theta_0 = 0°$ and near (θ,φ) = $(10°,0°)$ for $\theta_0 = 75°$. The latter can be verified with vertical profiles of the layer contributions to the total and polarised TOA reflectances. As an example, Fig. 11 shows those profiles for $\theta_0 = 0°$, demonstrating that, toward perpendicular scattering geometries, an increasing fraction of the polarised signal originates from the gas above the cloud.

The Venus results in Fig. 10 show that this planet appears much brighter in locally reflected light than Earth. The higher R_{11} values are primarily due to the larger cloud optical thickness. As on Earth, cloud droplet single scattering features leave distinct signatures in P_s of the locally reflected light, which can be seen to shift with increasing θ_0, as they are characteristic for given scattering angles. However, the increase of the polarisation that is due to Rayleigh scattering around a scattering angle of 90°, is less pronounced on Venus than on Earth. For example, for $\theta_0 = 0°$, P_s increases only at the largest viewing zenith angles. Despite Venus's large atmospheric pressure at surface level, the cloud deck reaches up to 70 km of altitude leaving little gas above the cloud for light to scatter from, as shown in Fig. 11. Instead, the signal is dominated by abundant unpolarised light multiply scattered in the upper parts of the Venusian clouds.

5 Summary, discussion, and outlook

Polarimetry is a powerful tool for characterising planetary atmospheres and surfaces. Radiative transfer simulations of total and polarised radiances are essential for designing, preparing, and operating spectro(polari)metric remote sensing instruments. Even for instruments that do not measure polarisation, accounting for polarisation in simulations is crucial for obtaining accurate total radiance calculations and for assessing potential errors due to an instrument's polarisation sensitivity if no polarisation scrambler is used. With the increasing spatial resolution of current and future Earth observation spectro(polari)meters, simulating 3D radiative transfer effects, such as cloud shadows, becomes increasingly important.

In this paper, we have presented the 3D radiative transfer code MONKI (Monte Carlo KNMI), which fully accounts for the polarisation of light at all orders of scattering. MONKI is written in Fortran-90 and is based on the Monte Carlo method. Rather than counting photons at the detector, MONKI uses the more efficient 'local estimation method,' which calculates the probability of scattering towards the detector at each scattering event. MONKI can compute both horizontally homogeneous and inhomogeneous (3D cloudy) scenes. It can operate both in forward mode (with photons propagating from the source to the detector) and in backward mode (with photons propagating in the opposite direction). Both modes converge to similar results in similar computation times.

[8] As Θ equals $180°$ minus the reflection angle (cf. Fig. 1).

https://doi.org/10.5194/egusphere-2025-2197
Preprint. Discussion started: 14 July 2025

We compared results of MONKI with benchmark results for polarised radiances in horizontally homogeneous atmospheres (de Haan et al., 1987) and thick Rayleigh-scattering atmospheres (Natraj and Hovenier, 2012). Additionally, we validated MONKI's 3D radiative transfer capabilities using benchmark results for polarised radiances from 3D clouds (Emde et al., 2018). In all cases, MONKI showed excellent agreement with the benchmark results.

Although MONKI is not the first code of its kind, it has subtle but fundamental differences from other Monte Carlo codes. A common limitation of Monte Carlo codes is their failure to converge in optically thick and strongly polarising atmospheres. This issue arises if approximations are made when propagating the polarisation state of photons during sampling of the scattering direction. MONKI, however, fully tracks the polarisation history of each photon along its trajectory, and therefore converges even in optically thick, strongly polarising planetary atmospheres. The derivations of our formulae are provided in the appendices.

The current version of MONKI does not use variance reduction techniques. Although such techniques can reduce the noise (and therefore the computation time needed for convergence), they can introduce biases (see, e.g. Barker et al., 2003) and/or increase code complexity. For example, directional importance sampling, which involves adjusting forward-peaked single scattering phase functions and photon weights, and photon splitting (see, e.g. Buras and Mayer, 2011), are mathematically correct but can reduce a code's intuitiveness. By omitting variance reduction techniques, MONKI produces unbiased results while preserving readability and simplicity, and thus adaptability when future extensions of the code are to be implemented. Instead of using such techniques, we increase the number of photons to achieve higher precision when needed.

In order to speed up MONKI's simulations, we implemented and presented a precomputation approach for optical paths to the detector. By precomputing the optical thickness of the horizontally homogeneous background gas for each atmospheric layer towards the detector, and by identifying grid cells that have cloud- and aerosol-free optical paths to the detector, MONKI avoids repeated photon propagations between the locations of the scattering events and the detector. This approach significantly improves computational efficiency, especially in scenes with low and/or patchy clouds, without compromising the accuracy.

We have presented sample signals of the TOA reflectance and degree of polarisation of light that is locally reflected by the Earth and Venus using horizontally homogeneous cloud models. This exercise demonstrated MONKI's versatility for various atmospheric conditions. For Earth applications, MONKI uses the same method as DAK (Doubling-Adding KNMI) to compute the input atmospheric optical properties. MONKI can import different particle scattering matrices and can, in principle, also simulate light scattered by non-spherical aerosol particles and ice clouds.

Since MONKI uses the Monte Carlo method, it can save the locations of photon scattering, also for different orders of scattering, for detailed analyses of features in the simulated signals. Among the planned extensions of MONKI is the implementation of atmospheric sphericity, which would allow computations for scenes with a low sun and/or large viewing angles. We conclude that MONKI is an accurate radiative transfer code, ready to support the design, preparation, and operations of spectro(polari)metric missions for Earth, Venus, and other planets.

https://doi.org/10.5194/egusphere-2025-2197
Preprint. Discussion started: 14 July 2025

Code availability. The version of MONKI as described in this paper is available from Zenodo under the Creative Commons Attribution 4.0 International licence. The version of the model used to produce the results presented in this paper (Trees, 2025), as well as the required input data, are archived under DOI (https://doi.org/10.5281/zenodo.15380811).

Appendix A: Describing the atmosphere and surface

In this appendix, we provide the formulae that describe the optical properties of the atmosphere and surface. Each grid cell in a MONKI simulation can contain gas and multiple aerosol types (e.g., cloud or haze droplets). For each cell, the Monte Carlo photon simulation requires the total optical thickness, b, the single scattering albedo, a, and the single scattering matrix, $\boldsymbol{F}$, separately for the gas and each aerosol type. The total optical thickness is the sum of the optical thicknesses of gas, b^{m}, and aerosols, b^{c}:

$$\begin{aligned} b(\lambda) &= b^{\mathrm{m}}(\lambda) + b^{\mathrm{c}}(\lambda) \\ &= b^{\mathrm{m}}_{\mathrm{sca}}(\lambda) + b^{\mathrm{m}}_{\mathrm{abs}}(\lambda) + b^{\mathrm{c}}_{\mathrm{sca}}(\lambda) + b^{\mathrm{c}}_{\mathrm{abs}}(\lambda), \end{aligned} \tag{A1}$$

where subscripts 'sca' and 'abs' denote scattering and absorption, respectively.

Single scattering of light by gas molecules is described by the anisotropic Rayleigh scattering matrix, $\boldsymbol{F}^{\mathrm{m}}$ (Hansen and Travis, 1974):

$$\boldsymbol{F}^{\mathrm{m}}(\Theta,\lambda) = \begin{bmatrix} F^{\mathrm{m}}_{11}(\Theta,\lambda) & F^{\mathrm{m}}_{12}(\Theta,\lambda) & 0 & 0 \\ F^{\mathrm{m}}_{21}(\Theta,\lambda) & F^{\mathrm{m}}_{22}(\Theta,\lambda) & 0 & 0 \\ 0 & 0 & F^{\mathrm{m}}_{33}(\Theta,\lambda) & 0 \\ 0 & 0 & 0 & F^{\mathrm{m}}_{44}(\Theta,\lambda) \end{bmatrix}. \tag{A2}$$

Here, Θ is the scattering angle, defined relative to the propagation direction of the incident light, such that $\Theta = 0^\circ$ corresponds to forward scattering and $\Theta = 180^\circ$ to backward scattering. The matrix elements of $\boldsymbol{F}^{\mathrm{m}}$ are given by:

$$F^{\mathrm{m}}_{11}(\Theta,\lambda) = \frac{3}{4}\Delta(\lambda)(1+\cos^2\Theta) + 1 - \Delta(\lambda), \tag{A3}$$

$$F^{\mathrm{m}}_{22}(\Theta,\lambda) = \frac{3}{4}\Delta(\lambda)(1+\cos^2\Theta), \tag{A4}$$

$$F^{\mathrm{m}}_{33}(\Theta,\lambda) = \frac{3}{2}\Delta(\lambda)\cos\Theta, \tag{A5}$$

$$F^{\mathrm{m}}_{44}(\Theta,\lambda) = \frac{3}{2}\Delta(\lambda)\Delta'(\lambda)\cos\Theta, \tag{A6}$$

$$F^{\mathrm{m}}_{12}(\Theta,\lambda) = F^{\mathrm{m}}_{21}(\Theta,\lambda) = -\frac{3}{4}\Delta(\lambda)\sin^2\Theta, \tag{A7}$$

with

$$\Delta(\lambda) = \frac{1-\delta(\lambda)}{1+\delta(\lambda)/2}, \qquad \Delta'(\lambda) = \frac{1-2\delta(\lambda)}{1-\delta(\lambda)}. \tag{A8}$$

https://doi.org/10.5194/egusphere-2025-2197
Preprint. Discussion started: 14 July 2025

The depolarisation factor, δ, is given by (Bodhaine et al., 1999):

$$\delta(\lambda) = \frac{6F_{\mathrm{k}}(\lambda) - 6}{7F_{\mathrm{k}}(\lambda) + 3}, \tag{A9}$$

where F_{k} is the so-called King correction factor, which depends on the mix of atmospheric gases.

In the current version of MONKI, gas properties are horizontally homogeneous, varying only with height, z. The scattering optical thickness for atmospheric layer k (between altitudes z_k^{bot} and z_k^{top}) is computed as (Stam et al., 2000):

$$b_{\mathrm{sca}}^{\mathrm{m}}(\lambda) = \frac{24\pi^3}{\lambda^4 N_L^2} \frac{(n^2(\lambda)-1)^2}{(n^2(\lambda)+2)^2} F_{\mathrm{k}}(\lambda) \frac{N_{\mathrm{av}}}{R} \int_{z_k^{\mathrm{bot}}}^{z_k^{\mathrm{top}}} \frac{p(z)}{T(z)} dz, \tag{A10}$$

where N_L is the Loschmidt number, N_{av} is Avogadro's constant, R is the universal gas constant, $n(\lambda)$ is the wavelength dependent refractive index of the atmospheric gas under standard conditions, and $p(z)$ and $T(z)$ are the vertical profiles of the ambient pressure and temperature, in Pa and K respectively. Given the vertical profiles of p and T at the layer boundaries z_k^{bot} and z_k^{top}, the integral is evaluated assuming an exponential decrease of p/T with z. Alternatively, if, for example, the temperature profile is unknown, $b_{\mathrm{sca}}^{\mathrm{m}}$ can be computed assuming hydrostatic equilibrium:

$$b_{\mathrm{sca}}^{\mathrm{m}}(\lambda) = \frac{24\pi^3}{\lambda^4 N_L^2} \frac{(n^2(\lambda)-1)^2}{(n^2(\lambda)+2)^2} F_{\mathrm{k}}(\lambda) \frac{N_{\mathrm{av}}}{M} \frac{\Delta p_k}{g}, \tag{A11}$$

where $\Delta p_k = p(z_k^{\mathrm{bot}}) - p(z_k^{\mathrm{top}})$, g is the gravitational acceleration, and M is the molecular mass of the background gas.

The gaseous absorption optical thickness for all n_{g} gases in atmospheric layer k is computed as follows (Stam et al., 2000):

$$b_{\mathrm{abs}}^{\mathrm{m}}(\lambda) = \sum_{i=1}^{n_{\mathrm{g}}} \frac{N_{\mathrm{av}}}{R} \int_{z_k^{\mathrm{bot}}}^{z_k^{\mathrm{top}}} \frac{p(z)}{T(z)} \eta_i(z) \sigma_{\mathrm{abs},i}^{\mathrm{m}}(\lambda, z) dz, \tag{A12}$$

where η_i is the volume mixing ratio of the absorbing gas with index i and $\sigma_{\mathrm{abs},i}^{\mathrm{m}}$ is its absorption cross section in m^2. The latter does not only depend on λ and i, but generally also on the ambient temperature and pressure inside the layer, hence the dependence on z. Between z_k^{bot} and z_k^{top}, we assume that η_i and $\sigma_{\mathrm{abs},i}^{\mathrm{m}}$ vary linearly with altitude. The single scattering albedo for the gas in a grid cell is defined as:

$$a^{\mathrm{m}}(\lambda) = \frac{b_{\mathrm{sca}}^{\mathrm{m}}(\lambda)}{b_{\mathrm{sca}}^{\mathrm{m}}(\lambda) + b_{\mathrm{abs}}^{\mathrm{m}}(\lambda)}. \tag{A13}$$

A light beam that interacts with an ensemble of aerosol particles is scattered and/or absorbed. Aerosol particles are spherical and defined by their size distributions and refractive index (Hansen and Travis, 1974). For a given wavelength and aerosol particle type, the single scattering albedo a^{c}, and the single scattering matrix $\boldsymbol{F}^{\mathrm{c}}$, are computed with Mie theory (de Rooij and van der Stap, 1984):

$$a^{\mathrm{c}}(\lambda) = \frac{b_{\mathrm{sca}}^{\mathrm{c}}(\lambda)}{b_{\mathrm{sca}}^{\mathrm{c}}(\lambda) + b_{\mathrm{abs}}^{\mathrm{c}}(\lambda)}, \tag{A14}$$

https://doi.org/10.5194/egusphere-2025-2197
Preprint. Discussion started: 14 July 2025

and

$$\boldsymbol{F}^{\mathrm{c}}(\Theta,\lambda) = \begin{bmatrix} F^{\mathrm{c}}_{11}(\Theta,\lambda) & F^{\mathrm{c}}_{12}(\Theta,\lambda) & 0 & 0 \\ F^{\mathrm{c}}_{21}(\Theta,\lambda) & F^{\mathrm{c}}_{22}(\Theta,\lambda) & 0 & 0 \\ 0 & 0 & F^{\mathrm{c}}_{33}(\Theta,\lambda) & F^{\mathrm{c}}_{34}(\Theta,\lambda) \\ 0 & 0 & F^{\mathrm{c}}_{43}(\Theta,\lambda) & F^{\mathrm{c}}_{44}(\Theta,\lambda) \end{bmatrix}, \tag{A15}$$

respectively, with $F^{\mathrm{c}}_{12} = F^{\mathrm{c}}_{21}$ and $F^{\mathrm{c}}_{43} = -F^{\mathrm{c}}_{34}$. The scattering and absorption optical thicknesses for an aerosol type at a given wavelength are:

$$b^{\mathrm{c}}_{\mathrm{sca}}(\lambda) = a^{\mathrm{c}}(\lambda)\sigma^{\mathrm{c}}(\lambda)N^{\mathrm{c}}, \tag{A16}$$

$$b^{\mathrm{c}}_{\mathrm{abs}}(\lambda) = (1 - a^{\mathrm{c}}(\lambda))\sigma^{\mathrm{c}}(\lambda)N^{\mathrm{c}}, \tag{A17}$$

where N^{c} is the aerosol particle column number density in m^{-2} and σ^{c} the particle extinction cross-section in m^2, the latter one also being computed with Mie theory. Each grid cell can contain multiple aerosol types and number densities, allowing the simulation of 3D cloud structures.

Instead of computing optical properties using the equations above, MONKI also allows prescribed input values for $b^{\mathrm{m}}_{\mathrm{sca}}$, $b^{\mathrm{m}}_{\mathrm{abs}}$, b^{c}, and δ. This feature is particularly useful for benchmarking against other radiative transfer codes.

In the current version of MONKI, the surface is assumed to reflect Lambertian. That is, the surface reflects isotropically and fully depolarising, with a specified albedo, A_{s}.

Appendix B: Sampling the free photon path length

This appendix, along with Appendices C, D, E, and F, concerns sampling techniques for randomly selecting a continuous variable based on its probability distribution (see, e.g., Dekking et al., 2005, for an introduction to probability theory). In MONKI, we use two techniques: the inverse transform method and the acceptance-rejection method (see Chap. 3 of Kroese et al., 2011).

Here, we describe how the inverse transform method is used to sample the free photon path length, d, until an atmospheric event (i.e., scattering or absorption) occurs. The inverse transform method requires (1) the cumulative distribution function (CDF) of d, denoted as $P(s)$[9], which gives the probability that the photon interacts within distance s, (2) a random number, ξ, uniformly distributed between 0 and 1, and (3) a solution for $d = P^{-1}(\xi)$, where P^{-1} is the inverse of P.

The direct transmittance, defined as the probability of a photon travelling along a straight distance s through an optically homogeneous medium with total extinction coefficient β, is given by $T_{\mathrm{dir}} = e^{-\beta s}$. In other words, this expression represents the probability that the photon does not encounter an event along distance s, or $\Pr(d > s)$ (see, e.g., Marshak and Davis, 2005). The probability that the photon does encounter an event before reaching distance s therefore equals:

$$\Pr(d \leq s) = 1 - e^{-\beta s}. \tag{B1}$$

[9]In the appendices of this paper, P denotes the CDF corresponding to a PDF p, and is not the degree of polarisation as in Sect. 2.1.

https://doi.org/10.5194/egusphere-2025-2197
Preprint. Discussion started: 14 July 2025

By definition, Eq. B1 is $P(s)$, the CDF for the free photon path length, d. To sample d, we generate a uniformly distributed random number $\xi \in (0,1)$ and compute (see also Eq. 9 of Mayer, 2009):

$$d = P^{-1}(\xi) = \frac{-\ln(1-\xi)}{\beta}. \tag{B2}$$

Since ξ is uniformly distributed in $(0,1)$, the transformation $\ln(1-\xi) \rightarrow \ln(\xi)$ is valid because both ξ and $1-\xi$ have identical probability density functions over this interval. Thus, Eq. B2 simplifies into (Eq. 4.39 of Marshak and Davis, 2005):

$$d = \frac{-\ln\xi}{\beta}. \tag{B3}$$

Sampling random values of d with Eq. B3 ensures that the sampled free photon path length follows an exponential distribution, which is consistent with the law of Lambert-Beer for radiative attenuation.

Appendix C: Sampling the surface reflection

In this Appendix, we show how to sample the direction (μ, φ) of a photon after it has been reflected by the Lambertian surface, that is, an isotropically and fully depolarising surface. Similarly as in App. B, we use the inverse transform method for this.

Suppose $\boldsymbol{I}$ is the radiance Stokes vector that has been reflected by a flat surface that reflects Lambertian. Consequently, only the first element of $\boldsymbol{I}$, I, is non-zero, and I will be independent of μ and φ. The reflected irradiance, or net flux, that emerges from the Lambertian surface then equals (see, e.g., Liou, 2002):

$$E = \int_0^{2\pi}\int_0^1 I\mu d\mu d\varphi = \pi I. \tag{C1}$$

Dividing both sides by πI gives

$$\int_0^{2\pi}\int_0^1 p(\mu,\varphi) d\mu d\varphi = 1, \tag{C2}$$

with

$$p(\mu,\varphi) = \frac{1}{\pi}\mu. \tag{C3}$$

Since $p(\mu,\varphi)$ is a function whose integrals equal 1, it is by definition the joint probability distribution function (PDF) of μ and φ. For Lambertian reflection, μ and φ are independent due to the symmetry in the azimuthal direction, such that $p(\mu,\varphi) = p(\mu)p(\varphi)$. Thus, the direction $(\mu,\ \varphi)$ can be sampled by sampling μ and φ individually from their marginal PDFs (see Sect. 3.2 of Kroese et al., 2011).

The marginal PDF of μ can be obtained by integrating Eq. C3 over φ:

$$p(\mu) = \int_0^{2\pi} p(\mu,\varphi) d\varphi = \int_0^{2\pi} \frac{1}{\pi}\mu d\varphi = 2\mu. \tag{C4}$$

https://doi.org/10.5194/egusphere-2025-2197
Preprint. Discussion started: 14 July 2025

The corresponding CDF is (see also Mayer, 2009, Eq. 18)

$$P(\mu) = \int_0^{\mu} p(\mu')d\mu' = 2\int_0^{\mu} \mu' d\mu' = \mu^2. \tag{C5}$$

The sampling expression for μ follows from the inverse of P (see also Mayer, 2009, Eq. 19):

$$\mu = P^{-1}(\xi_1) = \sqrt{\xi_1}, \tag{C6}$$

where ξ_1 is a generated, uniformly distributed random number between 0 and 1.

The marginal PDF of φ can be obtained by integrating Eq. C3 over μ:

$$p(\varphi) = \int_0^{1} p(\mu,\varphi)d\mu = \int_0^{1} \frac{1}{\pi}\mu d\mu = \frac{1}{2\pi}. \tag{C7}$$

The corresponding CDF is:

$$P(\varphi) = \int_0^{\varphi} p(\varphi')d\varphi' = \int_0^{\varphi} \frac{1}{2\pi} d\varphi' = \frac{\varphi}{2\pi}. \tag{C8}$$

The sampling expression for φ is then:

$$\varphi = P^{-1}(\xi_2) = 2\pi\xi_2, \tag{C9}$$

where ξ_2 is another generated uniformly distributed random number between 0 and 1.

Appendix D: The probability distribution of the atmospheric scattering direction of polarised light

In this Appendix, we derive the probability density function (PDF) of the scattering direction of light in a unit volume of atmosphere.

Let $\boldsymbol{I}'(\vartheta',\varphi')d\Omega'$ represent the flux vector of incident light at a unit volume in the atmosphere. The incident light may be polarised, described by vector $\boldsymbol{I}' = [I', Q', U', V']^T$, where $|Q'| > 0$, $|U'| > 0$ and/or $|V'| > 0$. The radiance vector of the scattered light is then (Hovenier et al., 2004, Eqs. 4.1 and 4.3):

$$\boldsymbol{I}(\vartheta,\varphi;\vartheta',\varphi') = \frac{a}{4\pi}\boldsymbol{Z}(\vartheta,\varphi;\vartheta',\varphi')\boldsymbol{I}'(\vartheta',\varphi')d\Omega'. \tag{D1}$$

whose first element, I, represents the total scattered radiance, or the energy scattered per unit solid angle, per unit wavelength interval, by the unit volume in the direction (ϑ,φ). Here, a is the single scattering albedo, and $\boldsymbol{Z}(\vartheta,\varphi;\vartheta',\varphi')$ is the phase matrix, given by $\boldsymbol{Z} = \boldsymbol{L}(-\sigma_2)\boldsymbol{F}(\Theta)\boldsymbol{L}(-\sigma_1)$ (Hovenier et al., 2004, Eq. 3.7). Matrices $\boldsymbol{F}$ and $\boldsymbol{L}$ are the single scattering matrix and the matrix for rotation of the polarisation reference plane, respectively, as in Eqs. 10 and 11.

https://doi.org/10.5194/egusphere-2025-2197
Preprint. Discussion started: 14 July 2025

To sample the scattering direction (ϑ, φ), it is convenient to first consider the scattered radiance vector after the rotation over angle σ_1 only, $\boldsymbol{I}^{\times}$, defined with respect to the scattering plane (see, e.g., the notes of Whitney, 2011):

$$\boldsymbol{I}^{\times}(\cos\Theta, \sigma_1; \vartheta', \varphi') = \frac{a}{4\pi}\boldsymbol{F}(\Theta)\boldsymbol{L}(-\sigma_1)\boldsymbol{I}'(\vartheta', \varphi')d\Omega'. \tag{D2}$$

Recall that in the case of Rayleigh and Mie scattering (and a few other special cases, see Hansen and Travis, 1974), the single scattering matrix elements $F_{13} = F_{14} = F_{24} = F_{23} = F_{31} = F_{32} = F_{41} = F_{42} = 0$ (see App. A). Substituting those values into Eq. D2 yields the following expression for the first element of $\boldsymbol{I}^{\times}$:

$$I^{\times}(\cos\Theta, \sigma_1; \vartheta', \varphi') = \frac{a}{4\pi}\Big[F_{11}(\Theta)I'(\vartheta', \varphi') + F_{12}(\Theta)\big(Q'(\vartheta', \varphi')\cos 2\sigma_1 - U'(\vartheta', \varphi')\sin 2\sigma_1\big)\Big]d\Omega'. \tag{D3}$$

Note that the value of $I^{\times}$ equals the total scattered radiance I, since the left multiplication by $\boldsymbol{L}(-\sigma_2)$ in Eq. D1 does not affect I. From inspection of Eq. D3 it is clear that I not only depends on the phase function F_{11}, but also on scattering matrix element F_{12} and on the state of polarisation of the light beam $\boldsymbol{I}'$ incident at the scattering volume.

Because of the conservation of energy, the total scattered radiance integrated over all scattering directions must equal the fraction a of the incident flux $I'd\Omega'$ that is being scattered:

$$\int_{-\pi}^{\pi}\int_{-1}^{1} I^{\times}(\cos\Theta, \sigma_1; \vartheta', \varphi')d\cos\Theta d\sigma_1 = aI'(\vartheta', \varphi')d\Omega'. \tag{D4}$$

Substituting Eq. D3 into Eq. D4 yields:

$$aI'(\vartheta', \varphi')d\Omega' \int_{-\pi}^{\pi}\int_{-1}^{1} \frac{1}{4\pi}\frac{1}{I'(\vartheta', \varphi')}\Big[F_{11}(\Theta)I'(\vartheta', \varphi') + F_{12}(\Theta)\big(Q'(\vartheta', \varphi')\cos 2\sigma_1 - U'(\vartheta', \varphi')\sin 2\sigma_1\big)\Big] d\cos\Theta\, d\sigma_1 = aI'(\vartheta', \varphi')d\Omega'. \tag{D5}$$

Dividing both sides by $aI'(\vartheta', \varphi')d\Omega'$ gives:

$$\int_{-\pi}^{\pi}\int_{-1}^{1} p(\cos\Theta, \sigma_1)d\cos\Theta d\sigma_1 = 1, \tag{D6}$$

with

$$p(\cos\Theta, \sigma_1) = \frac{1}{4\pi}\frac{1}{I'(\vartheta', \varphi')}\Big[F_{11}(\Theta)I'(\vartheta', \varphi') + F_{12}(\Theta)\big(Q'(\vartheta', \varphi')\cos 2\sigma_1 - U'(\vartheta', \varphi')\sin 2\sigma_1\big)\Big]. \tag{D7}$$

https://doi.org/10.5194/egusphere-2025-2197
Preprint. Discussion started: 14 July 2025

Since the integrals in Eq. D6 equal 1, $p(\cos\Theta, \sigma_1)$ is the joint PDF for the scattering direction $(\cos\Theta, \sigma_1)$ of polarised light incident on the scattering volume.[10] Given the functions for $F_{11}(\Theta)$ and $F_{12}(\Theta)$, and the values of the Stokes parameters of the incident beam $\boldsymbol{I}'$, the variables $\cos\Theta$ and σ_1 can be sampled with a sampling method using this PDF (see Apps. E and F).

Finally, the scattering direction angles ϑ and φ are determined from the sampled values $\cos\Theta$ and σ_1 using spherical trigonometry (see Fig. 1):

$$\vartheta = \arccos\left(\cos\vartheta' \cos\Theta + \sin\vartheta' \sin\Theta \cos\sigma_1\right), \tag{D8}$$

$$\varphi = \varphi' - \arccos\left(\frac{\cos\Theta - \cos\vartheta' \cos\vartheta}{\sin\vartheta' \sin\vartheta}\right) \cdot \mathrm{sign}(\sigma_1), \tag{D9}$$

where the multiplication by the sign of σ_1 is needed for the correct rotation direction of φ.

Appendix E: Sampling the Rayleigh scattering direction

In this Appendix, we describe how to sample the photon direction (ϑ, φ) after Rayleigh scattering of polarised light. Because finding the CDF, and its inverse, corresponding to $p(\cos\Theta, \sigma_1)$ (Eq. D7) is not straightforward, we do not use the inverse transform method. Instead, we use the acceptance-rejection method (see Sect. 3.1.5 of Kroese et al., 2011).

The acceptance-rejection method requires the determination of an envelope function $f(\cos\Theta, \sigma_1) = Cg(\cos\Theta, \sigma_1)$ for some constant $C \geq 1$, such that $f(\cos\Theta, \sigma_1) \geq p(\cos\Theta, \sigma_1)$ for all $\cos\Theta$ and σ_1. The function $g(\cos\Theta, \sigma_1)$ is called the proposal PDF. Then, the acceptance-rejection method is executed in three steps: (1) randomly sample $\cos\Theta$ and σ_1 from $g(\cos\Theta, \sigma_1)$, (2) generate a uniformly distributed random variable ξ between 0 and 1, and (3) accept the values of $\cos\Theta$ and σ_1 if $\xi\, f(\cos\Theta, \sigma_1) \leq p(\cos\Theta, \sigma_1)$, otherwise reject and return to step (1).

For Rayleigh scattering, we construct an envelope function by recognizing that $p(\cos\Theta, \sigma_1)$ (Eq. D7) is largest at $\Theta = 0°$, where $F_{12}^{\mathrm{m}} = 0$ (Eq. A7). For simplicity, we set the envelope function equal to this maximum value:

$$f(\cos\Theta, \sigma_1) = \frac{F_{11}^{\mathrm{m}}(0°)}{4\pi} = \frac{1}{4\pi}\left(\frac{3}{2}\Delta(\lambda) + 1 - \Delta(\lambda)\right). \tag{E1}$$

Since f is constant in $\cos\Theta$ and σ_1, the proposal PDF $g = f/C$ is constant and thus follows a uniform distribution in the $\cos\Theta, \sigma_1$-domain. Therefore, we can sample $\cos\Theta$ and σ_1 independently by generating uniformly distributed random values in the domains $(-1, 1)$ and $(-\pi, \pi)$, respectively. Then, we generate ξ, and compute $p(\cos\Theta, \sigma_1)$ from $\cos\Theta$, σ_1, $F_{11}^{\mathrm{m}}(\Theta)$, $F_{12}^{\mathrm{m}}(\Theta)$ and $\boldsymbol{I}'$ (Eq D7), thus fully preserving the history of the photon's polarisation state. If $\xi f(\cos\Theta, \sigma_1) \leq p(\cos\Theta, \sigma_1)$, $\cos\Theta$ and σ_1 are accepted. Otherwise, $\cos\Theta$ and σ_1 are rejected, and the steps listed above are repeated. Finally, with the accepted values for $\cos\Theta$ and σ_1, the angles ϑ and φ are computed with spherical trigonometry (Eqs. D8 and D9).

Appendix F: Sampling the Mie scattering direction

In this Appendix, we describe how to sample the photon direction (ϑ, φ) after Mie scattering of polarised light. Similarly as in App. E, we use the acceptance-rejection method.

[10] If the incident light is unpolarised, Eq. D7 simplifies to the well-known result $p(\cos\Theta, \varphi) = F_{11}(\Theta)/(4\pi)$ (see, e.g., Hansen and Travis, 1974).

https://doi.org/10.5194/egusphere-2025-2197
Preprint. Discussion started: 14 July 2025

For Mie scattering, it is generally inefficient to use a constant value for the envelope function f. That is because Mie scattering phase functions are strongly peaked in the forward scattering directions (see Fig. 9), resulting in a low acceptance rate for the generated scattering angles. Instead, we construct the following envelope function, for which it can be shown that it satisfies $f \geq p$ for all $\cos\Theta$ and σ_1:

$$f(\cos\Theta, \sigma_1) = \frac{1}{4\pi}\left(F_{11}^{\mathrm{c}}(\Theta) + |F_{12}^{\mathrm{c}}(\Theta)|\sqrt{2}\right). \tag{F1}$$

Note that here f is not constant but depends on Θ. In fact, f follows the PDF p (Eq. D7), which strongly varies with Θ, closely. This ensures a high acceptance rate of the generated scattering angles.

The proposal PDF g can be obtained from f as follows:

$$\begin{aligned} g(\cos\Theta, \sigma_1) &= \frac{1}{C} f(\cos\Theta, \sigma_1) \\ &= \frac{1}{4\pi C}\left(F_{11}^{\mathrm{c}}(\Theta) + |F_{12}^{\mathrm{c}}(\Theta)|\sqrt{2}\right), \end{aligned} \tag{F2}$$

where the normalizing constant C, which makes g a valid PDF whose integrals equal 1, is given by:

$$\begin{aligned} C &= \int_{-\pi}^{\pi}\int_{-1}^{1} f(\cos\Theta, \sigma_1) d\cos\Theta d\sigma_1 \\ &= \frac{1}{2}\int_{-1}^{1}\left(F_{11}^{\mathrm{c}}(\Theta) + |F_{12}^{\mathrm{c}}(\Theta)|\sqrt{2}\right) d\cos\Theta. \end{aligned} \tag{F3}$$

Quantities $\cos\Theta$ and σ_1 must be sampled from $g(\cos\Theta, \sigma_1)$. Equivalently, they can be sampled from the marginal PDF $g(\cos\Theta)$ and the conditional PDF $g(\sigma_1|\cos\Theta)$ of σ_1 given $\cos\Theta$ (Kroese et al., 2011, Sect. 3.2). We apply the inverse transform method for that, which requires determining the CDFs corresponding to these PDFs (see App. B).

The marginal PDF $g(\cos\Theta)$ can be obtained by integration over σ_1:

$$\begin{aligned} g(\cos\Theta) &= \int_{-\pi}^{\pi} g(\cos\Theta, \sigma_1) d\sigma_1 \\ &= \frac{1}{2C}\left(F_{11}^{\mathrm{c}}(\Theta) + |F_{12}^{\mathrm{c}}(\Theta)|\sqrt{2}\right), \end{aligned} \tag{F4}$$

and the conditional PDF $g(\sigma_1|\cos\Theta)$ is obtained with the product rule (see, e.g., Rice, 2007, Sect. 3.5.2):

$$g(\sigma_1|\cos\Theta) = \frac{g(\cos\Theta, \sigma_1)}{g(\cos\Theta)} = \frac{1}{2\pi}. \tag{F5}$$

It may be noted that, indeed, $g(\sigma_1|\cos\Theta)$ does not depend on $\cos\Theta$, such that $g(\sigma_1|\cos\Theta) = g(\sigma_1)$ with $g(\sigma_1)$ the marginal PDF of σ. That is, $\cos\Theta$ and σ_1 are independent in the probability distribution g.

https://doi.org/10.5194/egusphere-2025-2197
Preprint. Discussion started: 14 July 2025

The CDF corresponding to $g(\cos\Theta)$ is:

$$G(\cos\Theta) = \int_{-1}^{\cos\Theta} g(\cos\Theta')d\cos\Theta' = \frac{1}{2C}\int_{-1}^{\cos\Theta}\left(F_{11}^{c}(\Theta') + |F_{12}^{c}(\Theta')|\sqrt{2}\right)d\cos\Theta'. \tag{F6}$$

In order to evaluate Eq. F6, we precompute the expression for C and generate a lookup table (LUT) for $G(\cos\Theta)$ at a fine $\cos\Theta$-grid, using the available data for $F_{11}^{c}(\Theta)$ and $F_{12}^{c}(\Theta)$ as computed using Mie theory. According to the inverse transform method, the sampling expression for $\cos\Theta$ is:

$$\cos\Theta = G^{-1}(\xi_1), \tag{F7}$$

with G^{-1} the inverse of G, and ξ_1 a uniformly distributed random number between 0 and 1. The value $\cos\Theta$ in Eq. F7 that corresponds to ξ_1 can be retrieved directly from the LUT using linear interpolation of the G values between 0 and 1.

The CDF corresponding to $g(\sigma_1)$ is

$$G(\sigma_1) = \int_{-\pi}^{\sigma_1} g(\sigma_1')d\sigma_1' = \int_{-\pi}^{\sigma_1}\frac{1}{2\pi}d\sigma_1' = \frac{\sigma_1+\pi}{2\pi}. \tag{F8}$$

The sampling expression for σ_1 is:

$$\sigma_1 = G^{-1}(\xi_2) = 2\pi\xi_2 - \pi, \tag{F9}$$

where also ξ_2 is a uniformly distributed random number between 0 and 1.

Finally, we compute $p(\cos\Theta,\sigma_1)$ from $\cos\Theta$, σ_1 and the Stokes vector of the incident beam $\boldsymbol{I}'$ (Eq. D7), and generate the uniformly distributed random variable $\xi \in (0,1)$. If $\xi f(\cos\Theta,\sigma_1) \leq p(\cos\Theta,\sigma_1)$, the quantities $\cos\Theta$ and σ_1 are accepted; otherwise, they are rejected and the above steps are repeated. With the accepted values for $\cos\Theta$ and σ_1, angles ϑ and φ are computed using spherical trigonometry (Eqs. D8 and D9).

Appendix G: Validation of the TOA reflectance formula

In this Appendix, we explain the role of π and μ in the reflectance estimation formula (Eq. 14). This formula follows from the local estimation method (Marchuk et al., 1980), which we use in Sect. 2.3. A mathematical explanation of this method, for unpolarised light and all orders of scattering, is available in Marshak and Davis (2005) and Deutschmann et al. (2011), although the derivations are spread over multiple chapters and use different notations.

https://doi.org/10.5194/egusphere-2025-2197
Preprint. Discussion started: 14 July 2025

For simplicity, consider a horizontally homogeneous, single-layer atmosphere that is illuminated at TOA by a beam of unpolarised light in the direction $(\mu_0,\ \varphi_0)$. The reflected radiance at TOA in the direction $(\mu,\ \varphi)$ is $I(\mu,\mu_0,\varphi-\varphi_0)$. The albedo at TOA, A, is the ratio of the outgoing irradiance over the incoming irradiance and can be expressed in terms of the total TOA reflectance R_{11} as (Hovenier et al., 2004, Eq. 4.52):

$$A = \frac{1}{\pi}\int_0^{2\pi}\int_0^1 R_{11}(\mu,\mu_0,\varphi-\varphi_0)\mu d\mu d\varphi. \tag{G1}$$

The prefactor $1/\pi$ ensures that the reflected irradiance is normalised by the incident irradiance. The factor μ accounts for the projection effect, as radiance leaving TOA at an angle contributes less to outgoing irradiance due to the slanted projection of the horizontal TOA area element.

Now, consider an observer centered at $(\mu^\odot,\varphi^\odot)$, subtending a small solid angle $d\Omega^\odot = d\mu^\odot d\varphi^\odot$. The fraction of the total irradiance at TOA directed towards the observer is given by:

$$dA^\odot = \frac{1}{\pi}R_{11}(\mu^\odot,\mu_0,\varphi^\odot-\varphi_0)\mu^\odot d\mu^\odot d\varphi^\odot. \tag{G2}$$

This quantity also represents the probability that an injected photon at TOA is reflected back to TOA within $d\Omega^\odot$:

$$\Pr(\mu\in d\mu^\odot \wedge \varphi\in d\varphi^\odot) = p(\mu^\odot,\varphi^\odot)d\mu^\odot d\varphi^\odot, \tag{G3}$$

where p is the probability density function (PDF) of the photon reflection towards (μ,φ). Equating Eqs. G2 and G3, we obtain:

$$R_{11} = \frac{\pi}{\mu^\odot}p(\mu^\odot,\varphi^\odot), \tag{G4}$$

which indeed matches the first element of Eq. 14 if p is simulated with the Monte Carlo estimate $\sum_{j=1}^{M}\sum_{i=1}^{N}\Phi_{i,j}/N$, as defined in Sect. 2.3.

To illustrate the Monte Carlo process with a simple example, assume that the layer consists of vacuum ($\beta=0$), and that the surface reflects Lambertian with albedo A_s. Consequently, every injected photon reaches the surface, its weight is multiplied by the probability of reflection, A_s (see Sect. 2.3), and subsequently multiplied by the PDF of the reflection direction towards the observer, μ/π (Eq. 12), when computing the photon's contribution (Eq. 9). Finally, a new photon direction is sampled after reflection (App. C), and the photon travels upward leaving the domain. Thus, each photon reflects only once ($M=1$), and MONKI computes for all N photons:

$$p(\mu^\odot,\varphi^\odot) = \frac{\sum_{i=1}^{N}\Phi_i}{N} = \frac{\sum_{i=1}^{N}\frac{\mu^\odot}{\pi}A_s}{N} = \frac{\mu^\odot}{\pi}A_s. \tag{G5}$$

Substituting Eq. G5 into Eq. G4 yields the expected result:

$$R_{11} = A_s, \tag{G6}$$

confirming the correct formulation of Eq. 14.

https://doi.org/10.5194/egusphere-2025-2197
Preprint. Discussion started: 14 July 2025

Author contributions. VT coded MONKI from scratch, did all simulations (except for the ones done by JW and PS stated below) and wrote the manuscript. PW was closely involved in the development of MONKI and tested MONKI as a user. JW did the validation of MONKI against the benchmark results of Emde et al. (2018). PS did the simulations with DAK for the comparison with MONKI (Fig. S6). All authors reviewed the manuscript and were involved in the selection of the results presented in this paper.

Competing interests. The authors declare that they have no conflict of interest.

https://doi.org/10.5194/egusphere-2025-2197
Preprint. Discussion started: 14 July 2025

References

Anderson, G. P., Clough, S. A., Kneizys, F. X., Chetwynd, J. H., and Shettle, E. P.: AFGL Atmospheric Constituent Profiles (0–120 km), AFGL-TR-86-0110, Air Force Geophysics Laboratory, Hanscom Air Force Base, MA, environmental Research Papers, No. 954, 1986.

Bagnulo, S., Belskaya, I., Cellino, A., Kwon, Y. G., Muñoz, O., and Stam, D. M.: Polarimetry of Solar System minor bodies and planets: Polarimetry of Solar System minor bodies and planets, The Astronomy and Astrophysics Review, 32, 7, https://doi.org/10.1007/s00159-024-00157-w, 2024.

Barker, H. W., Goldstein, R. K., and Stevens, D. E.: Monte Carlo Simulation of Solar Reflectances for Cloudy Atmospheres., Journal of the Atmospheric Sciences, 60, 1881–1894, https://doi.org/10.1175/1520-0469(2003)060<1881:MCSOSR>2.0.CO;2, 2003.

Barlakas, V., Macke, A., and Wendisch, M.: SPARTA - Solver for Polarized Atmospheric Radiative Transfer Applications: Introduction and application to Saharan dust fields, Journal of Quantitative Spectroscopy and Radiative Transfer, 178, 77–92, https://doi.org/10.1016/j.jqsrt.2016.02.019, 2016.

Bass, A. M. and Paur, R. J.: The ultraviolet cross-sections of ozone. I. The measurements. II - Results and temperature dependence, in: Atmospheric ozone; Proceedings of the Quadrennial, edited by Zerefos, C. S. and Ghazi, A., pp. 606–616, 1985.

Bates, D. R.: Rayleigh scattering by air, Planetary and Space Science, 32, 785–790, https://doi.org/10.1016/0032-0633(84)90102-8, 1984.

Bodhaine, B. A., Wood, N. B., Dutton, E. G., and Slusser, J. R.: On Rayleigh Optical Depth Calculations, Journal of Atmospheric and Oceanic Technology, 16, 1854, https://doi.org/10.1175/1520-0426(1999)016<1854:ORODC>2.0.CO;2, 1999.

Breon, F. M. and Doutriaux-Boucher, M.: A Comparison of Cloud Droplet Radii Measured From Space, IEEE Transactions on Geoscience and Remote Sensing, 43, 1796–1805, https://doi.org/10.1109/TGRS.2005.852838, 2005.

Buras, R. and Mayer, B.: Efficient unbiased variance reduction techniques for Monte Carlo simulations of radiative transfer in cloudy atmospheres: The solution, Journal of Quantitative Spectroscopy and Radiative Transfer, 112, 434–447, https://doi.org/10.1016/j.jqsrt.2010.10.005, 2011.

Chandrasekhar, S.: Radiative transfer, Dover Publications, New York, 1960.

Collins, D. G., Blättner, W. G., Wells, M. B., and Horak, H. G.: Backward Monte Carlo Calculations of the Polarization Characteristics of the Radiation Emerging from Spherical-Shell Atmospheres, Applied Optics, 11, 2684–2696, https://doi.org/10.1364/AO.11.002684, 1972.

Cornet, C., C-Labonnote, L., and Szczap, F.: Three-dimensional polarized Monte Carlo atmospheric radiative transfer model (3DMCPOL): 3D effects on polarized visible reflectances of a cirrus cloud, Journal of Quantitative Spectroscopy and Radiative Transfer, 111, 174–186, https://doi.org/10.1016/j.jqsrt.2009.06.013, 2010.

Cornet, C., -Labonnote, L. C., Waquet, F., Szczap, F., Deaconu, L., Parol, F., Vanbauce, C., Thieuleux, F., and Riédi, J.: Cloud heterogeneity on cloud and aerosol above cloud properties retrieved from simulated total and polarized reflectances, Atmospheric Measurement Techniques, 11, 3627–3643, https://doi.org/10.5194/amt-11-3627-2018, 2018.

de Haan, J. F., Bosma, P. B., and Hovenier, J. W.: The adding method for multiple scattering calculations of polarized light, Astronomy & Astrophysics, 183, 371–391, 1987.

de Rooij, W. A. and van der Stap, C. C. A. H.: Expansion of Mie scattering matrices in generalized spherical functions, Astronomy and Astrophysics, 131, 237–248, 1984.

Deirmendjian, D.: Electromagnetic scattering on spherical polydispersions., American Elsevier Publishing Company, 1969.

Dekking, F., Kraaikamp, C., Lopuhaa, H., and Meester, L.: A modern introduction to probability theory and statistics, Springer Londen, https://doi.org/https://doi.org/10.1007/1-84628-168-7, 2005.

https://doi.org/10.5194/egusphere-2025-2197
Preprint. Discussion started: 14 July 2025

Deschamps, P. Y., Breon, F. M., Leroy, M., Podaire, A., Bricaud, A., Buriez, J. C., and Seze, G.: The POLDER mission: instrument characteristics and scientific objectives, IEEE Transactions on Geoscience and Remote Sensing, 32, 598–615, https://doi.org/10.1109/36.297978, 1994.

Deutschmann, T., Beirle, S., Frieß, U., Grzegorski, M., Kern, C., Kritten, L., Platt, U., Prados-Román, C., Puk ̧ı ̄te, J., Wagner, T., Werner, B., and Pfeilsticker, K.: The Monte Carlo atmospheric radiative transfer model McArtim: Introduction and validation of Jacobians and 3D features, Journal of Quantitative Spectroscopy and Radiative Transfer, 112, 1119–1137, https://doi.org/10.1016/j.jqsrt.2010.12.009, 2011.

Emde, C. and Mayer, B.: Errors induced by the neglect of polarization in radiance calculations for three-dimensional cloudy atmospheres, Journal of Quantitative Spectroscopy and Radiative Transfer, 218, 151–160, https://doi.org/10.1016/j.jqsrt.2018.07.001, 2018.

Emde, C., Buras, R., Mayer, B., and Blumthaler, M.: The impact of aerosols on polarized sky radiance: model development, validation, and applications, Atmospheric Chemistry and Physics, 10, 383–396, https://doi.org/10.5194/acp-10-383-2010, 2010.

Emde, C., Barlakas, V., Cornet, C., Evans, F., Wang, Z., Labonotte, L. C., Macke, A., Mayer, B., and Wendisch, M.: IPRT polarized radiative transfer model intercomparison project - Three-dimensional test cases (phase B), Journal of Quantitative Spectroscopy and Radiative Transfer, 209, 19–44, https://doi.org/10.1016/j.jqsrt.2018.01.024, 2018.

Evans, K. F.: The Spherical Harmonics Discrete Ordinate Method for Three-Dimensional Atmospheric Radiative Transfer., Journal of the Atmospheric Sciences, 55, 429–446, https://doi.org/10.1175/1520-0469(1998)055<0429:TSHDOM>2.0.CO;2, 1998.

Fauchez, T., Cornet, C., Szczap, F., Dubuisson, P., and Rosambert, T.: Impact of cirrus clouds heterogeneities on top-of-atmosphere thermal infrared radiation, Atmospheric Chemistry and Physics, 14, 5599–5615, https://doi.org/10.5194/acp-14-5599-201410.5194/acpd-13-27459-2013, 2014.

García Muñoz, A. and Mills, F. P.: Pre-conditioned backward Monte Carlo solutions to radiative transport in planetary atmospheres. Fundamentals: Sampling of propagation directions in polarising media, Astronomy and Astrophysics, 573, A72, https://doi.org/10.1051/0004-6361/201424042, 2015.

Gay, B., Vaillon, R., and Pınar Mengüç, M.: Polarization imaging of multiply-scattered radiation based on integral-vector Monte Carlo method, Journal of Quantitative Spectroscopy and Radiative Transfer, 111, 287–294, 2010.

Ghail, R., Ansan, V., Bovolo, F., Breuer, D., Campbell, B., and Kiefer, W.: EnVision assessment study report – Understanding why Earth's closest neighbour is so different (ESA/SCI(2021)1), European Space Agency, https://sci.esa.int/web/cosmic-vision/-/envision-assessment-study-report-yellow-book, 2021.

Hale, G. M. and Querry, M. R.: Optical Constants of Water in the 200-nm to 200-μm Wavelength Region, Applied Optics, 12, 555–563, https://doi.org/10.1364/AO.12.000555, 1973.

Hansen, J. E. and Hovenier, J. W.: Interpretation of the polarization of Venus., Journal of the Atmospheric Sciences, 31, 1137–1160, https://doi.org/10.1175/1520-0469(1974)031<1137:IOTPOV>2.0.CO;2, 1974.

Hansen, J. E. and Travis, L. D.: Light scattering in planetary atmospheres, Space Science Reviews, 16, 527–610, https://doi.org/10.1007/BF00168069, 1974.

Hasekamp, O. P.: Capability of multi-viewing-angle photo-polarimetric measurements for the simultaneous retrieval of aerosol and cloud properties, Atmospheric Measurement Techniques, 3, 839–851, https://doi.org/10.5194/amt-3-839-201010.5194/amtd-3-1229-2010, 2010.

Hasekamp, O. P., Fu, G., Rusli, S. P., Wu, L., Di Noia, A., Brugh, J. a. d., Landgraf, J., Martijn Smit, J., Rietjens, J., and van Amerongen, A.: Aerosol measurements by SPEXone on the NASA PACE mission: expected retrieval capabilities, Journal of Quantitative Spectroscopy and Radiative Transfer, 227, 170–184, https://doi.org/10.1016/j.jqsrt.2019.02.006, 2019.

https://doi.org/10.5194/egusphere-2025-2197
Preprint. Discussion started: 14 July 2025

Haus, R., Kappel, D., and Arnold, G.: Radiative heating and cooling in the middle and lower atmosphere of Venus and responses to atmospheric and spectroscopic parameter variations, Planetary and Space Science, 117, 262–294, https://doi.org/10.1016/j.pss.2015.06.024, 2015.

Hovenier, J. W. and van der Mee, C. V. M.: Fundamental relationships relevant to the transfer of polarized light in a scattering atmosphere, AAP, 128, 1–16, 1983.

Hovenier, J. W., Van Der Mee, C., and Domke, H., eds.: Transfer of polarized light in planetary atmospheres : basic concepts and practical methods, vol. 318 of *Astrophysics and Space Science Library*, https://doi.org/10.1007/978-1-4020-2856-4, 2004.

Karalidi, T., Stam, D. M., and Hovenier, J. W.: Flux and polarisation spectra of water clouds on exoplanets, Astronomy and Astrophysics, 530, A69, https://doi.org/10.1051/0004-6361/201116449, 2011.

Kemp, J., Henson, G., Steiner, C., Beardsley, I., and Powell, E.: The optical polarization of the Sun, measured at a sensitivity of parts in ten million, Nature, 328, https://doi.org/10.1038/328092a0, 1987.

Kroese, D. P., Taimre, T., and Botev, Z. I.: Handbook of Monte Carlo Methods, Wiley Series in Probability and Statistics, John Wiley & Sons, https://doi.org/10.1002/9781118014967, 2011.

Liou, K. N.: An Introduction to Atmospheric Radiation, Academic Press, San Diego, CA, 2nd edn., 2002.

Marbach, T., Riedi, J., Lacan, A., and Schlüssel, P.: The 3MI mission: multi-viewing-channel-polarisation imager of the EUMETSAT polar system: second generation (EPS-SG) dedicated to aerosol and cloud monitoring, in: Polarization Science and Remote Sensing VII, edited by Shaw, J. A. and LeMaster, D. A., vol. 9613 of *Society of Photo-Optical Instrumentation Engineers (SPIE) Conference Series*, p. 961310, https://doi.org/10.1117/12.2186978, 2015.

Marchand, R. and Ackerman, T.: Evaluation of radiometric measurements from the NASA Multiangle Imaging Spectroradiometer (MISR): Two- and three-dimensional radiative transfer modeling of an inhomogeneous stratocumulus cloud deck, Journal of Geophysical Research (Atmospheres), 109, D18208, https://doi.org/10.1029/2004JD004710, 2004.

Marchuk, G. I., Mikhailov, G. A., Nazaraliev, M. A., Darbinjan, R. A., Kargin, B. A., and Elepov, B. S.: The Monte Carlo Methods in Atmospheric Optics, vol. 12 of *Springer Series in Optical Sciences*, Springer-Verlag, Berlin, Heidelberg, https://doi.org/10.1007/978-3-540-35237-2, 1980.

Marshak, A. and Davis, A., eds.: 3D Radiative Transfer in Cloudy Atmospheres, Physics of Earth and Space Environments, Springer, Berlin, Heidelberg, https://doi.org/10.1007/3-540-28519-9, 2005.

Marshak, A., Platnick, S., VáRnai, T., Wen, G., and Cahalan, R. F.: Impact of three-dimensional radiative effects on satellite retrievals of cloud droplet sizes, Journal of Geophysical Research (Atmospheres), 111, D09207, https://doi.org/10.1029/2005JD006686, 2006.

Mayer, B.: Radiative transfer in the cloudy atmosphere, in: European Physical Journal Web of Conferences, vol. 1 of *European Physical Journal Web of Conferences*, p. 75, https://doi.org/10.1140/epjconf/e2009-00912-1, 2009.

McBride, B. A., Sienkiewicz, N., Xu, X., Puthukkudy, A., Fernandez-Borda, R., and Martins, J. V.: In-flight characterization of the Hyper-Angular Rainbow Polarimeter (HARP2) on the NASA PACE mission, in: Society of Photo-Optical Instrumentation Engineers (SPIE) Conference Series, edited by Babu, S. R., Hélière, A., and Kimura, T., vol. 13192 of *Society of Photo-Optical Instrumentation Engineers (SPIE) Conference Series*, p. 131920H, https://doi.org/10.1117/12.3033680, 2024.

Mishchenko, M. I. and Travis, L. D.: Satellite retrieval of aerosol properties over the ocean using polarization as well as intensity of reflected sunlight, Journal of Geophysical Research, 102, 16,989–17,013, https://doi.org/10.1029/96JD02425, 1997.

https://doi.org/10.5194/egusphere-2025-2197
Preprint. Discussion started: 14 July 2025

Mishchenko, M. I., Lacis, A. A., and Travis, L. D.: Errors induced by the neglect of polarization in radiance calculations for Rayleigh-scattering atmospheres., Journal of Quantitative Spectroscopy and Radiative Transfer, 51, 491–510, https://doi.org/10.1016/0022-4073(94)90149-X, 1994.

Moroz, V. I.: The Atmosphere of Venus, Space Science Reviews, 29, 3–127, https://doi.org/10.1007/BF00177144, 1981.

Natraj, V. and Hovenier, J. W.: Polarized Light Reflected and Transmitted by Thick Rayleigh Scattering Atmospheres, The Astrophysical Journal, 748, 28, https://doi.org/10.1088/0004-637X/748/1/28, 2012.

Natraj, V., Li, K.-F., and Yung, Y. L.: Rayleigh Scattering in Planetary Atmospheres: Corrected Tables Through Accurate Computation of X and Y Functions, The Astrophysical Journal, 691, 1909–1920, https://doi.org/10.1088/0004-637X/691/2/1909, 2009.

Neefs, E., Vandaele, A. C., De Cock, R., Erwin, J., Robert, S., Thomas, I. R., Berkenbosch, S., Jacobs, L., Bogaert, P., Beeckman, B., Brassine, A., Messios, N., De Donder, E., Bolsée, D., Pereira, N., Tackley, P., Gerya, T., Kögl, S., Kögl, P., Gröbelbauer, H. P., Wirz, F., Székely, G., Eaton, N., Roibás-Millán, E., Torralbo, I., Rubio-Arnaldo, H., Alvarez, J. M., Navajas Ortega, D., De Vos, L., Sørensen, R., Moelans, W., Algoedt, A., Blau, M., Stam, D., Renotte, E., Klinkenberg, P., Borguet, B., Thomas, S., Vervaeke, M., Thienpont, H., Castro, J. M., and Jimenez, J.: VenSpec-H spectrometer on the ESA EnVision mission: Design, modeling, analysis, Acta Astronautica, 226, 178–201, https://doi.org/10.1016/j.actaastro.2024.10.018, 2025.

Palmer, K. F. and Williams, D.: Optical constants of sulfuric acid; application to the clouds of Venus?, Applied Optics, 14, 208–219, https://doi.org/10.1364/AO.14.000208, 1975.

Peck, E. R. and Reeder, K.: Dispersion of Air*, Journal of the Optical Society of America (1917-1983), 62, 958, https://doi.org/10.1364/JOSA.62.000958, 1972.

Rice, J. A.: Mathematical Statistics and Data Analysis, Cengage Learning, Belmont, CA, 3rd edn., 2007.

Rossi, L., Berzosa-Molina, J., Desert, J. M., Fossati, L., García Muñoz, A., Haswell, C., Kabath, P., Kislyakova, K., Stam, D., and Vidotto, A.: Spectropolarimetry as a tool for understanding the diversity of planetary atmospheres, Experimental Astronomy, 54, 1187–1196, https://doi.org/10.1007/s10686-021-09813-w, 2022.

Seiff, A., Schofield, J. T., Kliore, A. J., Taylor, F. W., Limaye, S. S., Revercomb, H. E., Sromovsky, L. A., Kerzhanovich, V. V., Moroz, V. I., and Marov, M. Y.: Models of the structure of the atmosphere of Venus from the surface to 100 kilometers altitude, Advances in Space Research, 5, 3–58, https://doi.org/10.1016/0273-1177(85)90197-8, 1985.

Sneep, M. and Ubachs, W.: Direct measurement of the Rayleigh scattering cross section in various gases, Journal of Quantitative Spectroscopy and Radiative Transfer, 92, 293–310, https://doi.org/10.1016/j.jqsrt.2004.07.025, 2005.

Spada, F., Krol, M. C., and Stammes, P.: McSCIA: application of the Equivalence Theorem in a Monte Carlo radiative transfer model for spherical shell atmospheres, Atmospheric Chemistry & Physics, 6, 4823–4842, https://doi.org/10.5194/acp-6-4823-2006, 2006.

Spilling, D. and Thales, A.: The Multi Angle Polarimeter (MAP) on board ESA's Copernicus Carbon Dioxide Monitoring mission (CO2M), in: International Conference on Space Optics — ICSO 2020, edited by Cugny, B., Sodnik, Z., and Karafolas, N., vol. 11852, p. 118520R, International Society for Optics and Photonics, SPIE, https://doi.org/10.1117/12.2599174, 2021.

Stam, D. M.: Spectropolarimetric signatures of Earth-like extrasolar planets, Astronomy and Astrophysics, 482, 989–1007, https://doi.org/10.1051/0004-6361:20078358, 2008.

Stam, D. M. and Hovenier, J. W.: Errors in calculated planetary phase functions and albedos due to neglecting polarization, Astronomy and Astrophysics, 444, 275–286, https://doi.org/10.1051/0004-6361:20053698, 2005.

https://doi.org/10.5194/egusphere-2025-2197
Preprint. Discussion started: 14 July 2025

Stam, D. M., de Haan, J. F., Hovenier, J. W., and Stammes, P.: A fast method for simulating observations of polarized light emerging from the atmosphere applied to the oxygen-A band., Journal of Quantitative Spectroscopy and Radiative Transfer, 64, 131–149, https://doi.org/10.1016/S0022-4073(99)00009-6, 2000.

Stammes, P.: Spectral radiance modelling in the UV-visible range, IRS 2000: Current Problems in Atmospheric Radiation, edited by: Smith, W.L. and Timofeyev, Y.M., A. Deepak Publishing, Hampton, Virginia, pp. 385–388, 2001.

Stap, F. A., Hasekamp, O. P., Emde, C., and Röckmann, T.: Influence of 3D effects on 1D aerosol retrievals in synthetic, partially clouded scenes, Journal of Quantitative Spectroscopy and Radiative Transfer, 170, 54–68, https://doi.org/10.1016/j.jqsrt.2015.10.008, 2016a.

Stap, F. A., Hasekamp, O. P., Emde, C., and Röckmann, T.: Multiangle photopolarimetric aerosol retrievals in the vicinity of clouds: Synthetic study based on a large eddy simulation, Journal of Geophysical Research (Atmospheres), 121, 12,914–12,935, https://doi.org/10.1002/2016JD024787, 2016b.

Stevens, B., Moeng, C.-H., and Sullivan, P. P.: Large-Eddy Simulations of Radiatively Driven Convection: Sensitivities to the Representation of Small Scales., Journal of the Atmospheric Sciences, 56, 3963–3984, https://doi.org/10.1175/1520-0469(1999)056<3963:LESORD>2.0.CO;2, 1999.

Trees, V.: MONKI (Monte Carlo KNMI), https://doi.org/10.5281/zenodo.15380811, in *MONKI: a three-dimensional Monte Carlo simulator of total and polarised radiation reflected by planetary atmospheres* (1.0), 2025.

Trees, V. J. H. and Stam, D. M.: Blue, white, and red ocean planets. Simulations of orbital variations in flux and polarization colors, Astronomy and Astrophysics, 626, A129, https://doi.org/10.1051/0004-6361/201935399, 2019.

Trees, V. J. H. and Stam, D. M.: Ocean signatures in the total flux and polarization spectra of Earth-like exoplanets, Astronomy and Astrophysics, 664, A172, https://doi.org/10.1051/0004-6361/202243591, 2022.

Trees, V. J. H., Wang, P., Stammes, P., Tilstra, L. G., Donovan, D. P., and Siebesma, A. P.: DARCLOS: a cloud shadow detection algorithm for TROPOMI, Atmospheric Measurement Techniques, 15, 3121–3140, https://doi.org/10.5194/amt-15-3121-2022, 2022.

Trees, V. J. H., Wang, P., Stammes, P., Tilstra, L. G., Donovan, D. P., and Siebesma, A. P.: Cancellation of cloud shadow effects in the absorbing aerosol index retrieval algorithm of TROPOMI, Atmospheric Measurement Techniques, 18, 73–91, https://doi.org/10.5194/amt-18-73-2025, 2025.

van Amerongen, A., Rietjens, J., Campo, J., Dogan, E., Dingjan, J., Nalla, R., Caron, J., and Hasekamp, O.: SPEXone: a compact multi-angle polarimeter, in: International Conference on Space Optics — ICSO 2018, edited by Sodnik, Z., Karafolas, N., and Cugny, B., vol. 11180 of *Society of Photo-Optical Instrumentation Engineers (SPIE) Conference Series*, p. 111800L, https://doi.org/10.1117/12.2535940, 2019.

van de Hulst, H. C.: Light Scattering by Small Particles, Dover Publications, New York, 1981.

Vanderbilt, V., Grant, L., and Daughtry, C.: Polarization of light scattered by vegetation, Proceedings of the IEEE, 73, 1012–1024, https://doi.org/10.1109/PROC.1985.13232, 1985.

Várnai, T., Marshak, A., and Yang, W.: Multi-satellite aerosol observations in the vicinity of clouds, Atmospheric Chemistry and Physics, 13, 3899–3908, https://doi.org/10.5194/acp-13-3899-201310.5194/acpd-12-32039-2012, 2013.

Vaughan, S. R., Gebhard, T. D., Bott, K., Casewell, S. L., Cowan, N. B., Doelman, D. S., Kenworthy, M., Mazoyer, J., Millar-Blanchaer, M. A., Trees, V. J. H., Stam, D. M., Absil, O., Altinier, L., Baudoz, P., Belikov, R., Bidot, A., Birkby, J. L., Bonse, M. J., Brandl, B., Carlotti, A., Choquet, E., van Dam, D., Desai, N., Fogarty, K., Fowler, J., van Gorkom, K., Gutierrez, Y., Guyon, O., Haffert, S. Y., Herscovici-Schiller, O., Hours, A., Juanola-Parramon, R., Kleisioti, E., König, L., van Kooten, M., Krasteva, M., Laginja, I., Landman, R., Leboulleux, L., Mouillet, D., N'Diaye, M., Por, E. H., Pueyo, L., and Snik, F.: Chasing rainbows and ocean glints: Inner

https://doi.org/10.5194/egusphere-2025-2197
Preprint. Discussion started: 14 July 2025

working angle constraints for the Habitable Worlds Observatory, Monthly Notices of the Royal Astronomical Society, 524, 5477–5485, https://doi.org/10.1093/mnras/stad2127, 2023.

Veefkind, J. P., Aben, I., McMullan, K., Förster, H., de Vries, J., Otter, G., Claas, J., Eskes, H. J., de Haan, J. F., Kleipool, Q., van Weele, M., Hasekamp, O., Hoogeveen, R., Landgraf, J., Snel, R., Tol, P., Ingmann, P., Voors, R., Kruizinga, B., Vink, R., Visser, H., and Levelt, P. F.: TROPOMI on the ESA Sentinel-5 Precursor: A GMES mission for global observations of the atmospheric composition for climate, air quality and ozone layer applications, Remote Sensing of Environment, 120, 70–83, https://doi.org/10.1016/j.rse.2011.09.027, 2012.

Wang, Z., Cui, S., Yang, J., Gao, H., Liu, C., and Zhang, Z.: A novel hybrid scattering order-dependent variance reduction method for Monte Carlo simulations of radiative transfer in cloudy atmosphere, Journal of Quantitative Spectroscopy and Radiative Transfer, 189, 283–302, https://doi.org/10.1016/j.jqsrt.2016.12.002, 2017.

Waquet, F., Cornet, C., Deuzé, J. L., Dubovik, O., Ducos, F., Goloub, P., Herman, M., Lapyonok, T., Labonnote, L. C., Riedi, J., Tanré, D., Thieuleux, F., and Vanbauce, C.: Retrieval of aerosol microphysical and optical properties above liquid clouds from POLDER/PARASOL polarization measurements, Atmospheric Measurement Techniques, 6, 991–1016, https://doi.org/10.5194/amt-6-991-201310.5194/amtd-5-6083-2012, 2013.

Wen, G., Marshak, A., Levy, R. C., Remer, L. A., Loeb, N. G., Várnai, T., and Cahalan, R. F.: Improvement of MODIS aerosol retrievals near clouds, Journal of Geophysical Research (Atmospheres), 118, 9168–9181, https://doi.org/10.1002/jgrd.50617, 2013.

Werdell, P. J., Behrenfeld, M. J., Bontempi, P. S., Boss, E., Cairns, B., Davis, G. T., Franz, B. A., Gliese, U. B., Gorman, E. T., Hasekamp, O., Knobelspiesse, K. D., Mannino, A., Martins, J. V., McClain, C. R., Meister, G., and Remer, L. A.: The Plankton, Aerosol, Cloud, Ocean Ecosystem Mission: Status, Science, Advances, Bulletin of the American Meteorological Society, 100, 1775–1794, https://doi.org/10.1175/BAMS-D-18-0056.1, 2019.

Whitney, B. A.: Monte Carlo radiative transfer, in: Fluid Flows To Black Holes: A Tribute to S Chandrasekhar on His Birth Centenary. Edited by D. J. Saikia and Virginia Trimble., edited by Saikia, D. J. and Trimble, V., pp. 151–176, World Scientific Publishing Co. Pte. Ltd, https://doi.org/10.1142/9789814374774_0011, 2011.

Wilmouth, D. M. and Sayres, D. S.: Determination of Rayleigh scattering cross sections and indices of refraction for Ar, CO2, SF6, and CH4 using BBCES in the ultraviolet, Journal of Quantitative Spectroscopy and Radiative Transfer, 255, 107 224, https://doi.org/https://doi.org/10.1016/j.jqsrt.2020.107224, 2020.